

# Strength and Deformation of Rockfill Material Based on Large-Scale Triaxial Compression Tests. I: Influences of Density and Pressure

Yang Xiao, S.M.ASCE<sup>1</sup>; Hanlong Liu<sup>2</sup>; Yumin Chen<sup>3</sup>; and Jingshan Jiang<sup>4</sup>

**Abstract:** A series of large-scale triaxial compression tests were conducted to investigate the strength and deformation behaviors of Tacheng rockfill material (TRM) in relation to the initial void ratio and initial confining pressure. The critical state friction angle of TRM was expressed as a linear function of the logarithm of the initial confining pressure. The excess peak state friction angle and excess characteristic state friction angle of TRM were formulated as linear equations of a revised relative dilatancy index to capture the influences of density and pressure on the peak state and characteristic state friction angles. The initial elastic modulus, tangent modulus, and secant modulus of TRM were dependent on the initial void ratio and initial confining pressure. In addition, a formulation incorporating density and pressure was proposed to simulate the initial elastic modulus of TRM. The volumetric and deviatoric strains of TRM at the critical state were also dependent on density and pressure. The critical state line of TRM in the  $e - \lg p'$  space descended with a decrease in the initial void ratio. DOI: [10.1061/\(ASCE\)GT.1943-5606.0001176](https://doi.org/10.1061/(ASCE)GT.1943-5606.0001176). © 2014 American Society of Civil Engineers.

**Author keywords:** Rockfill material; Density; Pressure; Deformation; Strength; Friction angle; Modulus; Critical state line (CSL).

## Introduction

Rockfill material, as defined by Marsal (1967), Leps (1970), Marschi et al. (1972), Charles and Watts (1980), Barton and Kjaernsli (1981), and Matheson (1986), is composed of more than 50% coarse-grained soil larger than the No. 4 sieve size (ASTM 2006a). Rockfill material is widely used for the construction of rockfill dams (Cooke 1984; Dascal 1987; Khalid et al. 1990; Prato and Matheu 1991; Elgamal 1992; Uddin and Gazetas 1995; Hunter and Fell 2003; Milligan 2003; Papalou and Bielak 2004; Xing et al. 2006; Peiris et al. 2008; Costa and Alonso 2009; Seo et al. 2009; Flores-Berrones et al. 2011; Walberg et al. 2013) and railroads (Janardhanam and Desai 1983; Diyaljee 1987; Indraratna et al. 1998; Haque et al. 2007; Anderson and Fair 2008; Nimbalkar et al. 2012; Sevi and Ge 2012). Therefore, extensive experimental research on rockfill material has been conducted for the further application of rockfill in the construction of rockfill dams and railroads. These tests were mainly conducted using a large-scale triaxial apparatus (Marsal 1967; Leps 1970; Marschi et al. 1972; Charles and Watts 1980; Barton and Kjaernsli 1981; Varadarajan

et al. 1997; Indraratna et al. 1998; Varadarajan et al. 1999; Gupta 2000; Varadarajan et al. 2003, 2006; Anderson and Fair 2008; Gupta 2009a, b; Chu et al. 2010; Honkanadavar 2010; Honkanadavar and Gupta 2010; Seif El Dine et al. 2010; Honkanadavar et al. 2011; Araei et al. 2012; Honkanadavar et al. 2012; Sevi and Ge 2012; Vasistha et al. 2012; Xu et al. 2012; Vasistha et al. 2013; Xiao et al. 2014a, c). Furthermore, a multiaxial testing device at large capacities (Desai et al. 1982; Desai and Siriwardane 1983; Desai and Faruque 1984; Desai et al. 1995; Desai and Toth 1996; Desai 2001) was used to investigate the behavior of rockfill material (Janardhanam and Desai 1983; Desai and Salami 1987; Desai and El-Hoseiny 2005). True triaxial tests on rockfill materials were also conducted for different loading paths (Shi 2008; Xiao et al. 2011a, b, 2012).

The strength and deformation behavior of sand depends on density and pressure. Been and Jeffries (1985) proposed a state parameter to capture the influence of density and pressure on the strength and deformation behavior of sand. Other state parameters for sand include the following: (1) the state index combining the current void ratio and critical state void ratio, which was proposed by Ishihara (1993); (2) the state index expressed by the ratio of the current void ratio to critical state void ratio, which was proposed by Wan and Guo (1999); and (3) the state index combining the current mean effective stress and critical mean effective stress, which was proposed by Wang et al. (2002). Research on the state-dependent behaviors and modeling of sand (Been and Jefferies 1985; Gudehus 1996; Li 1997; Li and Wang 1998; Gajo and Muir Wood 1999; Wan and Guo 1999; Li and Dafalias 2000, 2002; Wang et al. 2002; Yang and Li 2004; Yao et al. 2004; Lashkari 2009; Loukidis and Salgado 2009) has been conducted in recent decades. Cho et al. (2006) found that the particle shape could influence the packing density, stiffness, and strength of sands considerably. Honkanadavar (2010) investigated the state-dependent behaviors of the strength and stress-strain relationship of rockfill materials through a series of large-scale triaxial tests. Hu et al. (2010) conducted a series of triaxial compression tests on rockfill materials at various gradations and confining pressures.

The main objective of this paper is to systemically investigate the influence of density and pressure on the strength and deformation of

<sup>1</sup>Associate Professor, College of Civil Engineering, Chongqing Univ., Chongqing 400450, China; Researcher, College of Civil and Transportation Engineering, Hohai Univ., Nanjing 210098, China. E-mail: hhxyanson@163.com

<sup>2</sup>Professor and Chair, College of Civil Engineering, Chongqing Univ., Chongqing 400450, China. E-mail: cehliu@cqu.edu.cn

<sup>3</sup>Associate Professor, College of Civil and Transportation Engineering, Hohai Univ., Nanjing 210098, China (corresponding author). E-mail: ymchenhhu@163.com

<sup>4</sup>Lecturer, School of Civil Engineering, Nanjing Institute of Technology, Nanjing 211167, China. E-mail: jingshanjiang@yahoo.com

Note. This manuscript was submitted on June 19, 2013; approved on July 15, 2014; published online on August 21, 2014. Discussion period open until January 21, 2015; separate discussions must be submitted for individual papers. This paper is part of the *Journal of Geotechnical and Geoenvironmental Engineering*, © ASCE, ISSN 1090-0241/04014070(16)/\$25.00.

rockfill material through a series of large-scale triaxial compression tests. The strength and deformation indexes influenced by density and pressure include the following: (1) friction angle (e.g., mobilized friction angle, critical state friction angle, peak state friction angle, characteristic state friction angle); (2) modulus (e.g., initial elastic modulus, tangent modulus, secant modulus); (3) stress-strain relationship; (4) volumetric and deviatoric strains at the critical state; and (5) critical state line (CSL).

## Large-Scale Triaxial Compression Tests

### Material

Tacheng rockfill material (TRM) for testing was obtained from the Tacheng Hydropower Station located in Shangrila County in the western part of China (Jiang 2009). Specific details of the study site are presented in Table 1. The prototype TRM is an alluvium material consisting of rounded/subrounded particles up to 200 mm in size. The particle size of the prototype TRM was reduced by the parallel gradation technique (Lowe 1964), with a maximum particle size of 60 mm. Table 2 presents the basic properties of TRM, for example the mineralogy, unconfined compressive strength (ASTM 2010a), maximum flat and elongated (ASTM 2010b), uncompacted void content (ASTM 2006d), aggregate impact value [European Committee for Standardization (CEN) 2010], aggregate crushing value (CEN 2010), and Los Angeles abrasion value (ASTM 2006b, 2012b).

**Table 1.** Project and Site for TRM

Project detail	Depiction
Project name	Tacheng Hydropower Station
Dam type	High earth core rockfill dam
Site	Shangrila County, Yunnan Province, China
Rocks of TRM	Gravel, pebble, boulder, and shingle

**Table 2.** Basic Characteristics of TRM

Characteristics	Descriptions or values
Rockfill source	Alluvium
Mineralogy	Gritstone, sandstone, conglomerate, marble, claystone, schist, quartzite, and granite
Unconfined compressive strength (MPa) (ASTM 2010a)	106.5
Particle shape	Rounded/subrounded with $D > 10$ mm Angular/subangular with $D < 10$ mm
Maximum flat and elongated (percentage) (ASTM 2010b)	9.5
Uncompacted void content (percentage) (ASTM 2006d)	46.3
Aggregate impact value (percentage) (CEN 2010)	29.2
Aggregate crushing value (percentage) (CEN 2010)	39.2
Los Angeles abrasion value (percentage) (ASTM 2006b, 2012b)	25.8

The TRM particles were subangular when the particle size was less than 10 mm, as shown in Figs. 1(a and b), whereas the TRM particles were rounded and subrounded when the particle size was more than 10 mm, as illustrated in Figs. 1(c–e). The mixed material is shown in Fig. 1(f). The initial grading (IG) of TRM for testing is similar to the prototype grading (PG) of TRM, as shown in Fig. 2(a). Fig. 2(b) presents the distributions of each TRM particle size. Table 3 provides the basic values of the characteristic particle sizes, for example the maximum particle diameter  $D_{max}$ , mean particle diameter  $D_{50}$ , uniformity coefficient  $C_u$ , coefficient of curvature  $C_c$ , percentage of coarse fraction larger than the No. 4 sieve size (i.e., PCF4) (ASTM 2006a), and percentage of material with particle size smaller than the No. 200 sieve size [i.e., fines content (FC)] (ASTM 2006a). The TRM used for testing is classified as Unified Soil Classification System's well-graded gravels (GW) according to ASTM (2006a), with  $PCF4 > 50$ ,  $FC < 5$ ,  $C_u > 4$ , and  $1 < C_c < 3$ . Table 4 provides the values of the specific gravity  $G_s$ , relative density, and dry density of TRM.

Fig. 2(a) illustrates that the maximum diameter of the PG (i.e., 200 mm) is greater than that of the IG (i.e., 60 mm). An increase in particle size would lead to more cracks and defects in the particles (McDowell et al. 1996; McDowell and Bolton 1998), indicating that the PG sample has a lower strength than the IG sample. All of the tests in this paper were conducted with IG samples using a parallel gradation technique. Therefore, the test results could not be directly used for the prototype material for the construction of dams. Nevertheless, the original work by Frossard et al. (2012) made it possible to evaluate the strength of rockfill material with large particles based on the material strength of the rockfill material's small particles with parallel grading. The investigation of the strength of TRM using Frossard's method will be discussed in future work.

### Large-Scale Triaxial Apparatus

A simplified diagram of a large-scale triaxial apparatus (LSTA) is presented in Fig. 3. The confining pressure was applied by the air-water pressure system, with a maximum pressure of 3 MPa. The axial load was applied by the oil hydraulic system, with a maximum axial load of 1,500 kN. In this paper, the tests were performed at a constant axial displacement of 1 mm/min. The axial deviatoric load was measured by a load cell, and the axial deformation was measured by a digital dial gauge attached to the piston. The volumetric strain was derived from the expelled water. The triaxial compression test data for TRM were recorded automatically. Details of the LSTA are presented in Table 5.

### Specimen Preparation and Testing Procedure

The initial confining pressures of the TRM used for testing were 0.4, 0.8, and 1.6 MPa. These pressures are typical for the Tacheng Rockfill Dam. For each confining pressure, there were four specimens with initial void ratios of 0.189, 0.244, 0.285, and 0.317, as listed in Table 5, yielding a total of 12 specimens.

The cylinder specimen was 300 mm in diameter and 600 mm high. The quantity for each particle size was determined by the weight to obtain the IG of TRM to prepare the sample at a specific density, as listed in Table 4. The samples were prepared with a measurement accuracy of 0.01 g using a split mold with mixed material (wetting with a moisture content of 3–5%), as shown in Fig. 1(f). A 3-mm-thick rubber membrane was placed inside the split mold to wrap the specimen. Filter stones were used at both ends, as shown in Fig. 4(a). The mixed material was divided into five equal parts for compaction inside the split mold. Each layer of the

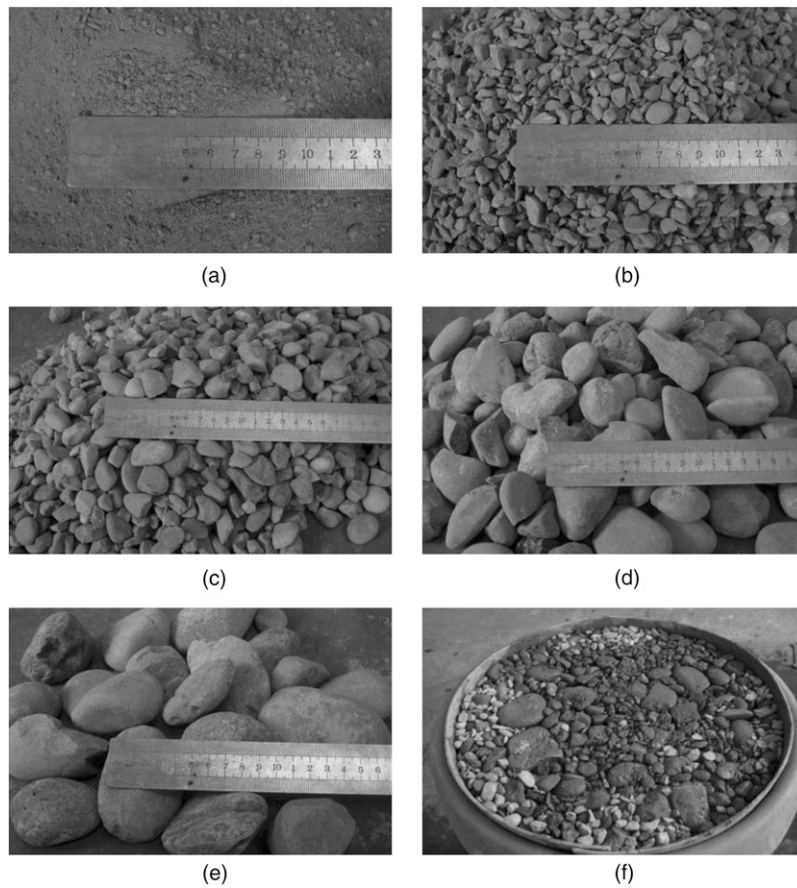


Fig. 1. Sample components and compaction (reprinted from Xiao et al. 2014a, © ASCE)

specimen was compacted using a vibrator with a frequency of 70 cycles per second. The specimen was sealed by latex rubber rings at each end, as shown in Fig. 4(a), and subsequently saturated using the vacuum saturation method, with a  $B$  value in excess of 0.96. The installed apparatus is shown in Fig. 4(b).

After reaching saturation, the specimen was subjected to the required confining pressure. Then, the specimen was sheared under the drained condition with a constant axial strain rate of 1 mm/min. The test was stopped when the accumulated axial strain reached 15%. Based on the test results, the volumetric strain and stress ratio changed only slightly at an axial strain of 15%, indicating that the soil parameters at this axial strain can be regarded as the critical state parameters (Roscoe et al. 1963). In all of the tests, high strain levels were reached by bulging without an obvious shear plane, as shown in Fig. 5.

The test results presented and discussed in the following sections include the following: (1) friction angle (e.g., mobilized friction angle, critical state friction angle, peak state friction angle, characteristic state friction angle); (2) modulus (e.g., initial elastic modulus, tangent modulus, secant modulus); (3) stress-strain relationship; (4) volumetric and deviatoric strains at the critical state; and (5) CSL.

## Friction Angle

### Mobilized Friction Angle

The strength of TRM is influenced by density and pressure in a rather complicated manner. The friction angle of TRM is first investigated

according to the triaxial test data. According to the critical state soil mechanism (Schofield and Wroth 1968), the mobilized friction angle  $\phi_m$  under the triaxial compression condition is defined as

$$\sin \phi_m = \frac{3\eta}{6 + \eta} \quad (1)$$

The stress ratio  $\eta$  in Eq. (1) is defined as the ratio of the deviatoric stress  $q$  to the mean effective stress  $p'$

$$\eta = \frac{q}{p'} \quad (2)$$

where  $p'$  and  $q$  under the triaxial compression condition are defined as

$$p' = \frac{\sigma'_1 + \sigma'_2 + \sigma'_3}{3} = \frac{\sigma'_1 + 2\sigma'_3}{3} \quad (3a)$$

$$\begin{aligned} q &= \frac{1}{\sqrt{2}} \sqrt{(\sigma'_1 - \sigma'_2)^2 + (\sigma'_2 - \sigma'_3)^2 + (\sigma'_3 - \sigma'_1)^2} \\ &= \sigma'_1 - \sigma'_3 \end{aligned} \quad (3b)$$

where  $\sigma'_1$ ,  $\sigma'_2$ , and  $\sigma'_3$  = major, intermediate, and minor effective principal stresses, respectively.

The critical state friction angle  $\phi_{cs}$  under the triaxial compression condition can be defined as

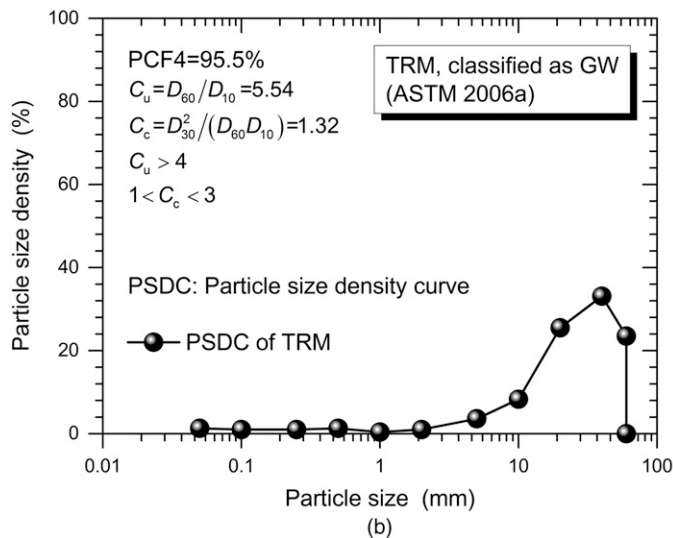
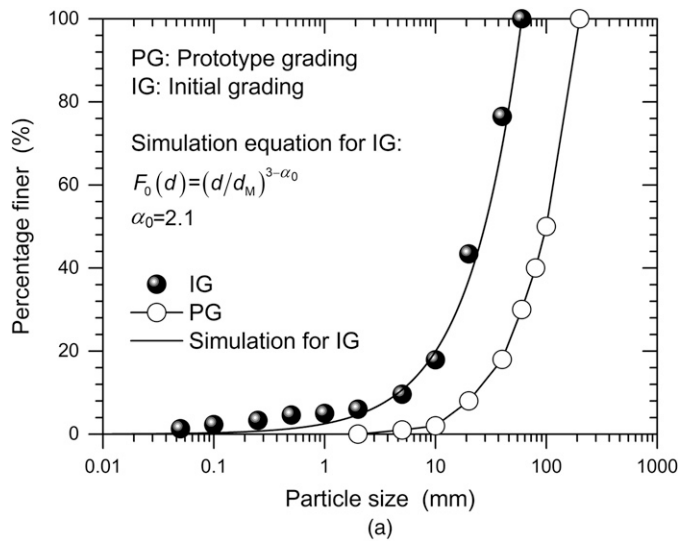


**Fig. 2.** TRM used in the large-scale triaxial tests: (a) particle-size distribution; (b) particle-size density curve

**Table 3.** Particle-Size Analysis of TRM

Characteristics (ASTM 2006c)	Values
$D_{max}$ (mm)	60.0
$D_{50}$ (mm)	23.1
$C_u$	5.54
$C_c$	1.32
PCF4 (percentage)	95.5
FC (percentage)	1.8

Note: TRM is classified under Unified Soil Classification System's well-graded gravels (GW) (ASTM 2006a) because  $PCF4 > 50$ ,  $FC < 5$ ,  $C_u > 4$ , and  $1 < C_c < 3$ .

$$\sin \phi_{cs} = \frac{3\eta_{cs}}{6 + \eta_{cs}} \quad (4)$$

where  $\eta_{cs}$  = critical state stress ratio. The value of  $\eta_{cs}$  is constant based on the framework of the critical state soil mechanics. The values of  $\phi_{cs}$  for TRM at different densities and pressures can be

**Table 4.** Density of TRM

Characteristics	Values
Specific gravity	
$G_s$	2.69
Relative density (ASTM 2012a)	
$I_D$	0.84 for $e_0 = 0.189$ 0.70 for $e_0 = 0.244$ 0.59 for $e_0 = 0.285$ 0.51 for $e_0 = 0.317$
Dry density (ASTM 2012a)	
$\rho_{max}$ ( $10^3$ kg/m <sup>3</sup> )	2.38
$\rho_{min}$ ( $10^3$ kg/m <sup>3</sup> )	1.79
$\rho_d$ ( $10^3$ kg/m <sup>3</sup> )	2.27 for $e_0 = 0.189$ 2.17 for $e_0 = 0.244$ 2.10 for $e_0 = 0.285$ 2.05 for $e_0 = 0.317$

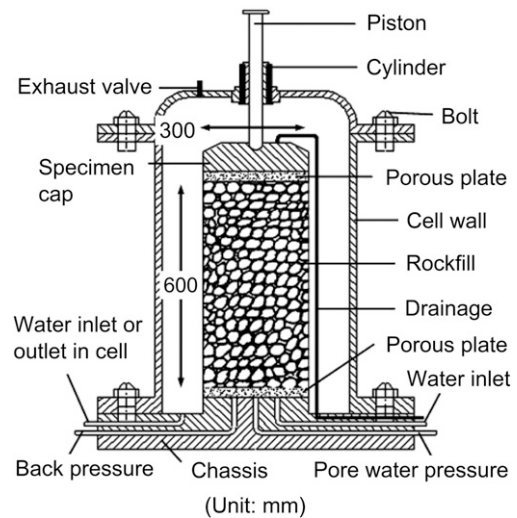


**Fig. 3.** Simplified diagram of the LSTA for TRM

**Table 5.** Details of the LSTA and Specimen Preparation

Details	Descriptions or values
<b>LSTA</b>	
Specimen size	Length = 600 mm, diameter = 300 mm
Maximum confining pressure (MPa)	3
Loading mode of confining pressure	Air-water pressure system
Maximum axial load (kN)	1,500
Mode of the axial load	Oil hydraulic system
Axial strain rate used (mm/min)	1
<b>Specimen preparation</b>	
Initial confining pressure (MPa)	0.4, 0.8, and 1.6
Initial void ratio	0.189, 0.244, 0.285, and 0.317
Total number of tests	12
Material of the membrane	Rubber
Thickness of the membrane (mm)	3
Number of membranes in each test	1
Compaction method	Vibration
Frequency of the vibration in the sample preparation (cycles per second)	70
$B$ value after saturation	0.96

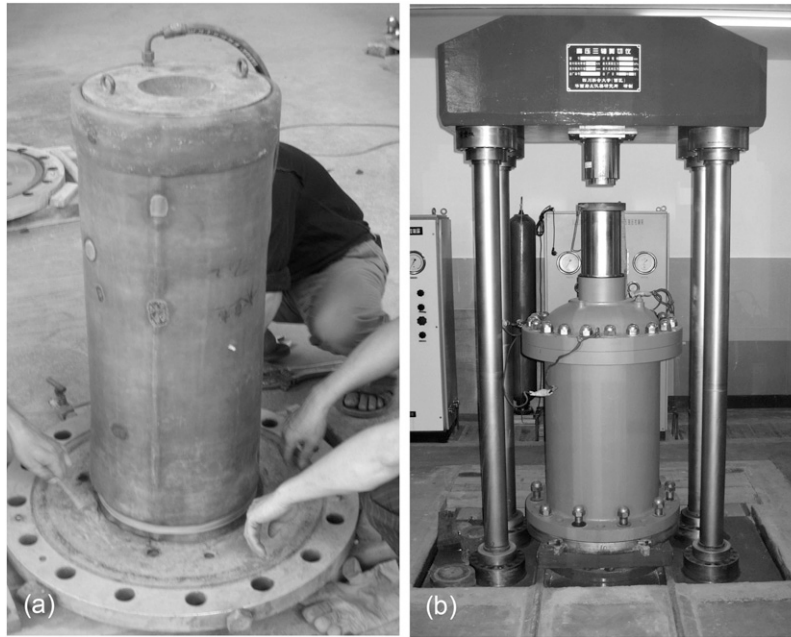


**Fig. 4.** LSTA and sample preparation procedure (reprinted from Xiao et al. 2014c, © ASCE): (a) installation of the sample; (b) installation of the apparatus



**Fig. 5.** Bulging failure mode of TRM (reprinted from Xiao et al. 2014c, © ASCE)

determined by the test data at the critical state. According to the test results, the volumetric strain and stress ratio change only slightly at an axial strain of 15%, indicating that the state at this axial strain can be approximated as the critical state based on the critical state soil mechanics (Roscoe et al. 1963).

The characteristic state or phase-transformation state (Tatsuoka and Ishihara 1974; Ishihara et al. 1975; Luong 1980; Been and Jefferies 1985; Ishihara 1993) is defined as a condition under which the incremental volumetric strain is zero. The characteristic state friction angle  $\phi_{chs}$  under the triaxial compression condition is defined as

$$\sin \phi_{chs} = \frac{3\eta_{chs}}{6 + \eta_{chs}} \quad (5)$$

where  $\eta_{chs}$  = characteristic state stress ratio. The values of  $\phi_{chs}$  for TRM at different densities and pressures can be obtained from the test data at the characteristic state, at which the incremental volumetric strain is zero.

The peak state friction angle  $\phi_{ps}$  is defined as

$$\sin \phi_{ps} = \frac{3\eta_{ps}}{6 + \eta_{ps}} \quad (6)$$

where  $\eta_{ps}$  = peak state stress ratio during the shearing process. The values of  $\phi_{ps}$  for TRM at different densities and pressures can be obtained from the test data at the peak failure state, at which the stress ratio is maximum. For a dense state,  $\phi_m$  first turns to  $\phi_{chs}$  at the characteristic state, then to  $\phi_{ps}$  at the peak failure state, and finally to  $\phi_{cs}$  at the critical state in the shearing process.

Fig. 6 presents the mobilized friction angle of TRM at different densities and pressures. For a lower initial confining pressure, as shown in Fig. 6(a), the mobilized friction angle  $\phi_m$  increases with increasing axial strain up to a characteristic state friction angle  $\phi_{chs}$  (Been and Jefferies 1985). Then, the mobilized friction angle  $\phi_m$  increases to a peak state friction angle  $\phi_{ps}$ . The mobilized friction angle  $\phi_m$  decreases with increasing axial strain and then converges to the critical state friction angle  $\phi_{cs}$ . For higher initial confining pressure, as shown in Fig. 6(c), the mobilized friction angle increases proportionally to the critical state friction angle  $\phi_{cs}$ . Table 6 presents the values of the critical state friction angle  $\phi_{cs}$ , peak state friction

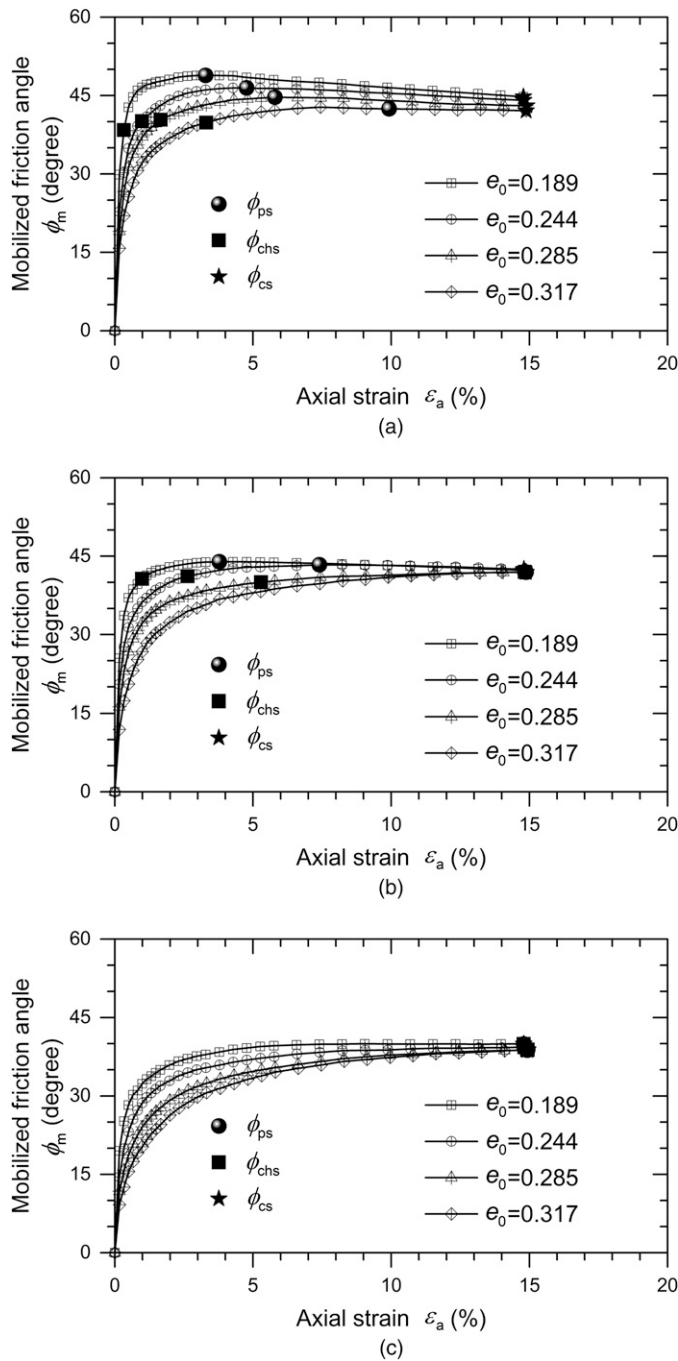


**Fig. 6.** Mobilized friction angle of TRM: (a)  $p_0 = 0.4$  MPa; (b)  $p_0 = 0.8$  MPa; (c)  $p_0 = 1.6$  MPa

angle  $\phi_{ps}$ , and characteristic state friction angle  $\phi_{chs}$  at different initial confining pressures and initial void ratios.

### Critical State Friction Angle

Figs. 6 and 7 illustrate that the initial void ratio  $e_0$  has a minor influence on the critical state friction angle  $\phi_{cs}$ . In contrast, as shown in Fig. 7, the initial confining pressure  $p_0$  has a considerable influence on the critical state friction angle  $\phi_{cs}$ . As a result, the critical state friction angle  $\phi_{cs}$  is only correlated with the initial confining pressure  $p_0$ . As shown in Fig. 7, the relationship between

the critical state friction angle  $\phi_{cs}$  and initial confining pressure  $p_0$  can be given as

$$\phi_{cs} = \phi_{cs0} - \phi_{csd} \ln(p_0/p_a) \quad (7)$$

where  $\phi_{cs0}$  and  $\phi_{csd}$  = material constants. The formulation [Eq. (7)] was also proposed to describe the friction angle of other rockfill materials (Barton and Kjaemli 1981; Xu et al. 2012; Fu et al. 2014).

### Peak State Friction Angle

Fig. 8 illustrates that the peak state friction angle  $\phi_{ps}$  varies with the initial confining pressure  $p_0$  and initial void ratio  $e_0$ . An increase in either the initial confining pressure  $p_0$  or initial void ratio  $e_0$  would lead to a decrease in the peak friction angle  $\phi_{ps}$ .

Rowe (1962) proposed a stress-dilatancy equation for sands to depict the relationship between the peak state friction angle, critical state friction angle, and dilatancy angle. Based on the experiment data of 17 sands, a relative dilatancy index was proposed by Bolton (1986) to describe the friction angle in relation to density and pressure

$$I_R = I_D [Q - \ln(p')] - R \quad (8)$$

where  $Q$  and  $R$  = state index constants of the material;  $p'$  = mean effective stress at failure; and relative density  $I_D$  can be expressed as

$$I_D = \frac{e_{\max} - e}{e_{\max} - e_{\min}} \quad (9)$$

where  $e$  = void ratio;  $e_{\min}$  = minimum void ratio; and  $e_{\max}$  = maximum void ratio.

Chakraborty and Salgado (2010) found that the coefficient of the stress-dilatancy equation is constant for both triaxial-compression and plane-strain conditions. Based on a series of direct shear tests on sand-gravel mixtures, Simoni and Houlsby (2006) supposed that the stress-dilatancy equation is in relation to the gravel fraction.

A revised relative dilatancy index is proposed using the atmospheric pressure for normalization in the same units as  $p'$ . The revised index can be expressed as

$$I_{RR} = I_D [Q - \ln(p'/p_a)] - R \quad (10)$$

The values of  $Q$  and  $R$  in Eq. (10) are presented in Table 9. The excess peak state friction angle  $\phi_{ps}^{ex} = (\phi_{ps} - \phi_{cs})$  can be expressed as a linear formulation of the revised state index  $I_{RR}$  as

$$\phi_{ps}^{ex} = \phi_{ps} - \phi_{cs} = \alpha_{\phi} I_{RR} \quad (11)$$

where coefficient  $\alpha_{\phi}$  = ratio between the excess peak state friction angle  $\phi_{ps}^{ex}$  and revised state index  $I_{RR}$  (Table 9).

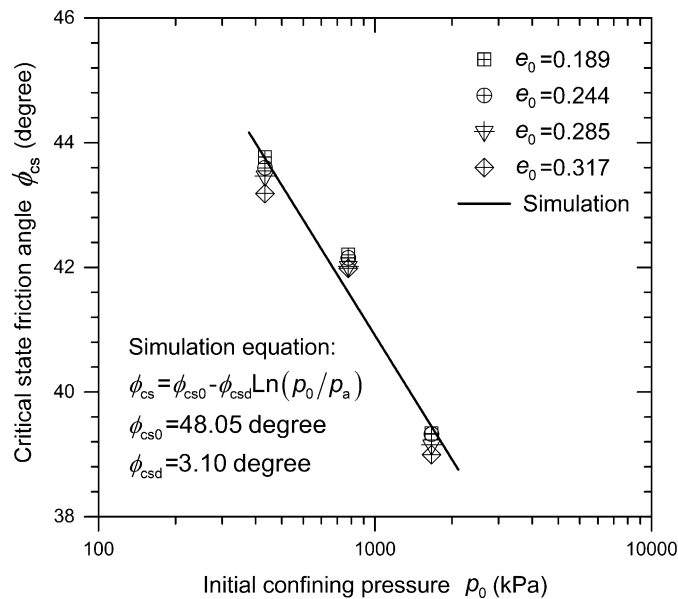
Fig. 9 illustrates that the simulation by Eq. (11) agrees well with the test data of TRM in terms of the relationship between the excess peak state friction angle  $\phi_{ps}^{ex}$  and revised state index  $I_{RR}$ .

### Characteristic State Friction Angle

As shown in Fig. 10, the excess characteristic state friction angle  $\phi_{chs}^{ex} = (\phi_{cs} - \phi_{chs})$  can be expressed by a linear formulation of the revised state index  $I_{RR}$  as

**Table 6.** Critical State Friction Angle, Peak State Friction Angle, and Characteristic State Friction Angle of TRM

Initial confining pressure ( $p_0$ ) (MPa)	Initial void ratio ( $e_0$ )	Critical state friction angle ( $\phi_{cs}$ ) (degrees)	Peak state friction angle ( $\phi_{ps}$ ) (degrees)	Characteristic state friction angle ( $\phi_{chs}$ ) (degrees)
0.4	0.189	44.77	48.85	38.39
	0.244	44.09	46.46	40.08
	0.285	43.06	44.67	40.36
	0.317	42.09	42.46	39.81
0.8	0.189	42.30	43.93	40.66
	0.244	42.50	43.35	41.15
	0.285	41.93	41.93	39.99
	0.317	41.99	41.99	41.98
1.6	0.189	39.93	39.98	39.93
	0.244	39.33	39.34	39.33
	0.285	38.74	38.74	38.74
	0.317	38.86	38.86	38.86

**Fig. 7.** Variations in the critical state friction angle of TRM with the initial confining pressure

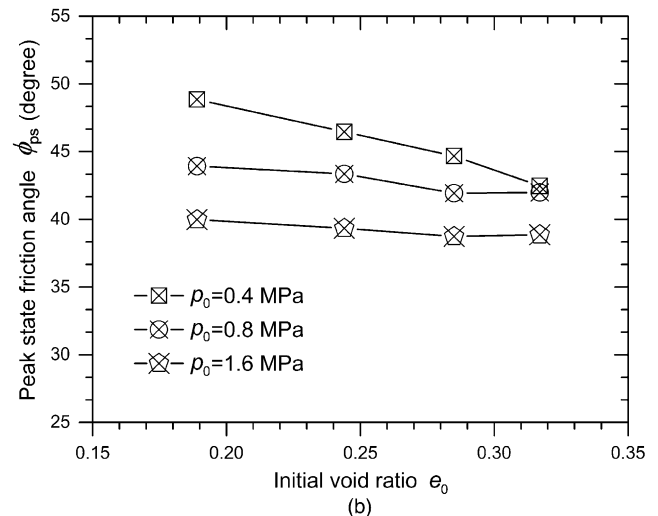
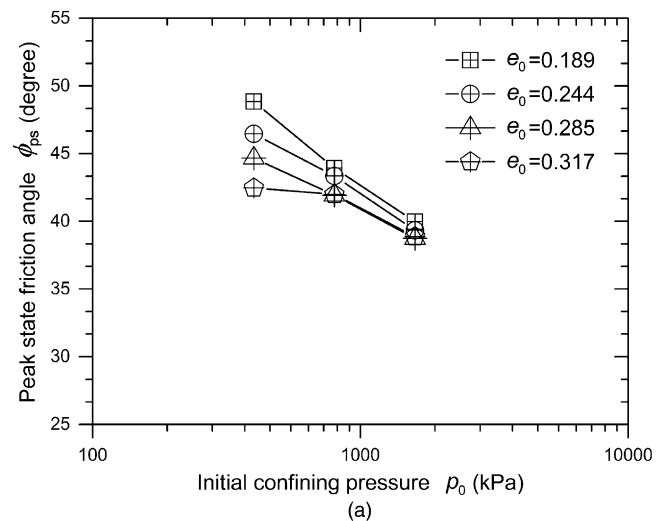
$$\phi_{chs}^{ex} = \phi_{cs} - \phi_{chs} = \beta_{\phi} I_{RR} \quad (12)$$

where coefficient  $\beta_{\phi}$  = ratio between the excess characteristic state friction angle  $\phi_{chs}^{ex}$  and  $I_{RR}$  (Table 9). As shown in Fig. 10, Eq. (12) can be used to simulate the test data of TRM in terms of the relationship between the excess characteristic state friction angle  $\phi_{chs}^{ex}$  and revised state index  $I_{RR}$ .

## Modulus

### Initial Elastic Modulus

The initial elastic modulus of TRM is an important parameter, indicating the deformation behavior of TRM. The initial slope of the stress-strain curve ( $q - \varepsilon_a$ ) is used to determine the initial elastic modulus  $E_{0i}$ . The axial strain is constrained within 0.1% for the initial slope of the stress-strain curve, where the deformation is supposed to be elastic. Table 7 provides the values of the initial elastic modulus  $E_{0i}$  of TRM at different initial confining pressures

**Fig. 8.** Variations in the peak state friction angle of TRM: (a) initial confining pressure; (b) initial void ratio

and initial void ratios. As shown in Fig. 11(a), the initial elastic modulus  $E_{0i}$  of TRM at a given initial void ratio increases with an increase in the initial confining pressure  $p_0$ , whereas the  $E_{0i}$  of TRM decreases with an increase in the initial void ratio  $e_0$  at a given initial confining pressure, as shown in Fig. 11(b). Therefore, the initial

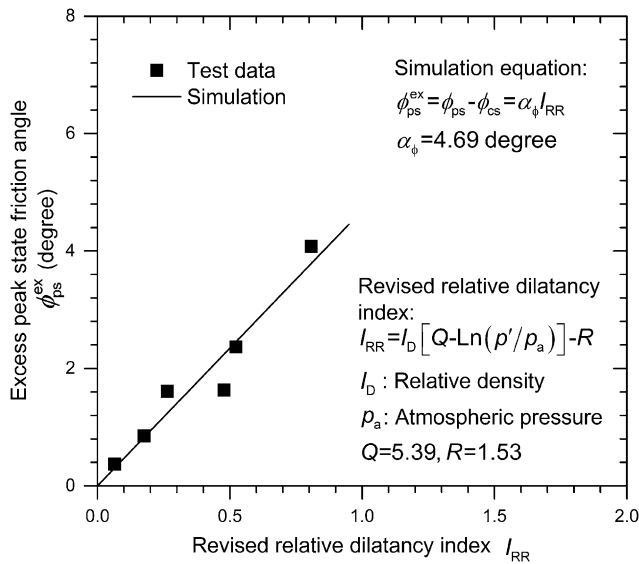


**Fig. 9.** Relationship between the excess peak state friction angle  $\phi_{ps}^{ex}$  and revised relative dilatancy index  $I_{RR}$  for TRM

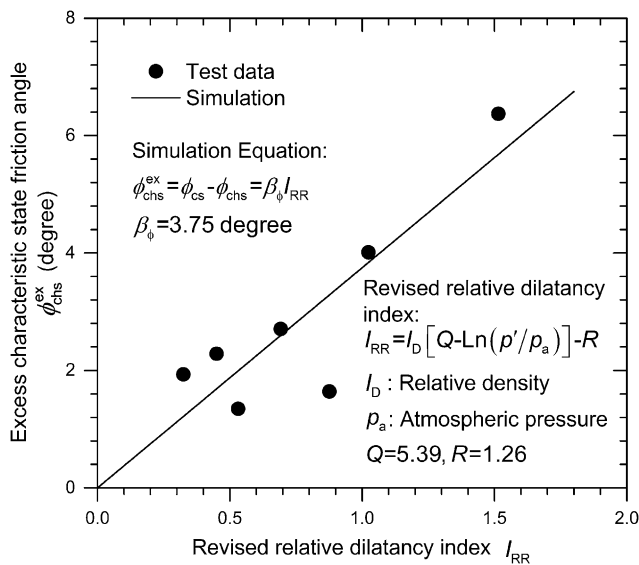


**Fig. 10.** Relationship between the excess characteristic state friction angle  $\phi_{chs}^{ex}$  and revised relative dilatancy index  $I_{RR}$  for TRM

elastic modulus  $E_{0i}$  is correlated with both the initial confining pressure  $p_0$  and initial void ratio  $e_0$ . An appropriate equation is proposed for the initial elastic modulus  $E_{0i}$  of TRM pertaining to the initial confining pressure  $p_0$  and initial void ratio  $e_0$ . The equation can be expressed as

$$E_{0i} = E_a (e_E + e_0)^{-\alpha_E} p_a (p_0/p_a)^{1-\beta_E} \quad (13)$$

where  $E_a$  = material constant (i.e., modulus coefficient) (Table 9);  $e_E$  and  $\alpha_E$  = material constants in relation to the initial void ratio (Table 9); and  $\beta_E$  = material constant in relation to the initial confining pressure (Table 9).

As shown in Fig. 11, the initial elastic modulus simulated by Eq. (13) agrees well with the test data pertaining to the initial confining pressure  $p_0$  and initial void ratio  $e_0$ .

### Tangent Modulus

The initial elastic modulus  $E_{0i}$  is actually the initial value of the tangent modulus  $E_t$ . Fig. 12 illustrates the variation of the tangent modulus  $E_t$  of TRM with the deviatoric stress  $q$  throughout the shearing process. As shown in Fig. 12, the tangent modulus  $E_t$  of TRM at a given initial void ratio and given initial confining pressure decreases with increasing in the deviatoric stress  $q$ . An increase in the initial void ratio  $e_0$  leads to a decrease in the tangent modulus  $E_t$  of TRM at a given deviatoric stress and given initial confining pressure. In addition, the comparisons in Figs. 12(a-c) indicate that an increase in the initial confining pressure results in an increase in the tangent modulus  $E_t$  of TRM at a given deviatoric stress and given initial void ratio.

### Secant Modulus

Similar to the tangent modulus  $E_t$ , the secant modulus  $E_s$  of TRM is also related to density and pressure. The secant modulus  $E_{50}$  at 50% of the peak strength is considered an important model parameter (Duncan and Chang 1970). As shown in Fig. 13, the secant modulus  $E_{50}$  at 50% of the peak strength is defined as the gradient of the secant line that goes through the origin point and the point at half of the peak deviatoric stress

$$E_{50} = 0.5q_{ps}/\epsilon_{aps} \quad (14a)$$

for strain-softening behavior

$$E_{50} = 0.5q_{cs}/\epsilon_{acs} \quad (14b)$$

**Table 7.** Initial Elastic Modulus and Secant Modulus at 50% of the Peak Strength of TRM

Initial confining pressure ( $p_0$ ) (MPa)	Initial void ratio ( $e_0$ )	Initial elastic modulus ( $E_{0i}$ ) (MPa)	Secant modulus at 50% of the peak strength ( $E_{50}$ ) (MPa)
0.4	0.189	483.31	414.24
	0.244	307.67	219.02
	0.285	233.79	160.92
	0.317	180.56	99.15
0.8	0.189	734.65	633.91
	0.244	524.38	349.08
	0.285	376.79	214.69
	0.317	252.99	110.69
1.6	0.189	974.13	582.85
	0.244	648.12	319.79
	0.285	494.71	178.52
	0.317	366.92	122.58

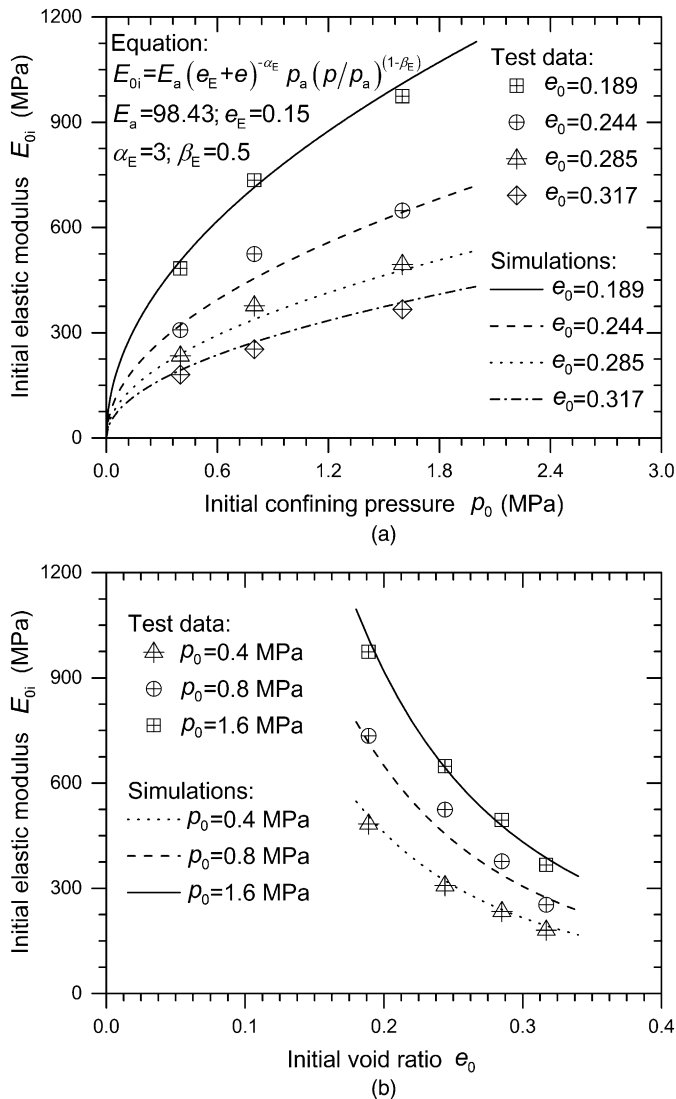


**Fig. 11.** Variations in the initial elastic modulus of TRM: (a) initial confining pressure; (b) initial void ratio

for strain-hardening behavior, where  $q_{ps}$  = deviatoric stress at the peak state;  $\varepsilon_{aps}$  = axial strain at the peak state;  $q_{cs}$  = deviatoric stress at the critical state; and  $\varepsilon_{acs}$  = axial strain at the critical state. Table 7 presents the values of  $E_{50}$  on TRM at different initial confining pressures and initial void ratios.

Fig. 14 presents the variation in the secant modulus  $E_s$  of TRM with deviatoric stress at different initial void ratios and initial confining pressures. For strain-softening behavior, the secant modulus  $E_s$  of TRM decreases with increasing deviatoric stress up to the peak failure state and then decreases with decreasing deviatoric stress. For strain-hardening behavior, the secant modulus  $E_s$  of TRM decreases with increasing deviatoric stress during shearing. Figs. 14(a and c) illustrates the definitions of  $E_{50}$  for strain-softening and strain-hardening behaviors, respectively. The circle points in Fig. 14 denote the secant modulus  $E_{50}$  at 50% of the peak strength.

As shown in Fig. 15(a), the  $E_{50}$  of TRM at  $e_0 = 0.189, 0.244,$  and  $0.285$  increases with an increase in the initial confining pressure and then decreases slightly with an increase in the initial confining pressure  $p_0$ . In contrast,  $E_{50}$  of TRM at  $e_0 = 0.317$  increases slightly with an increase in the initial confining pressure  $p_0$ , as shown in

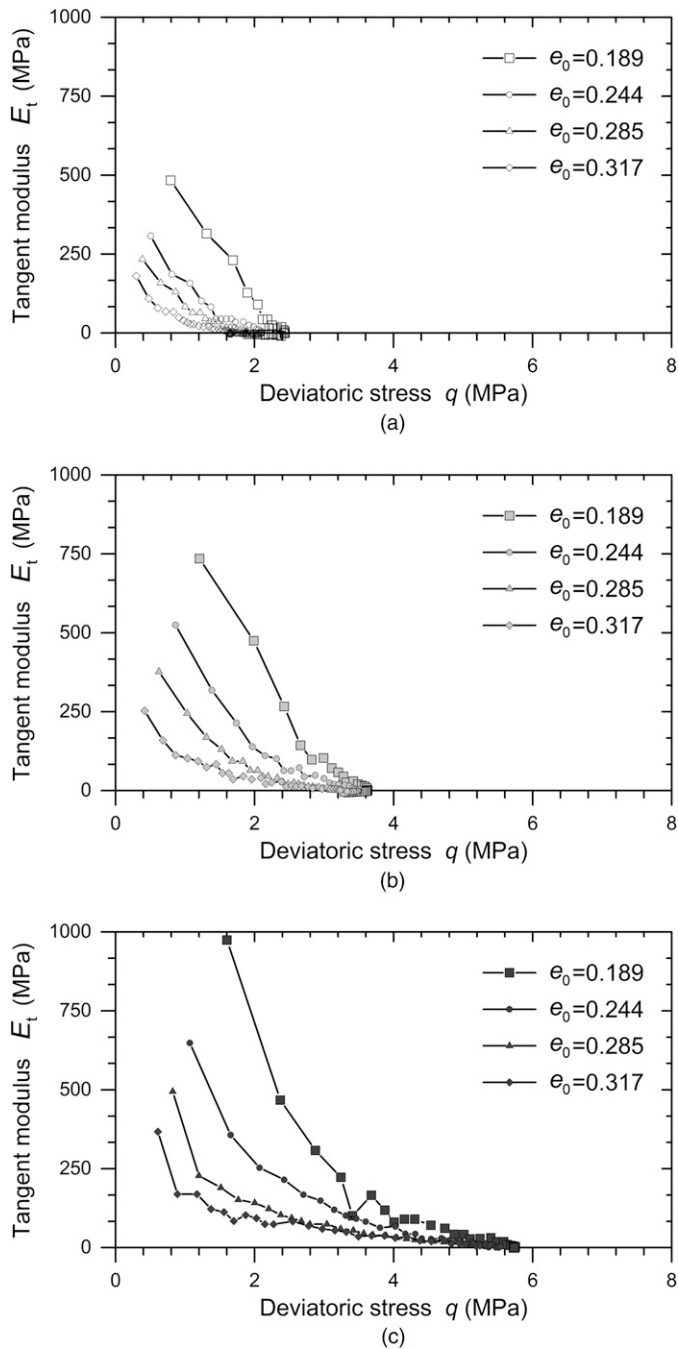


**Fig. 12.** Tangent modulus of TRM: (a)  $p_0 = 0.4$  MPa; (b)  $p_0 = 0.8$  MPa; (c)  $p_0 = 1.6$  MPa

Fig. 15(a). TRM at  $e_0 = 0.189, 0.244,$  and  $0.285$  produces the strain softening and volumetric expansion behaviors at a lower pressure (e.g.,  $p_0 = 0.4$  or  $0.8$  MPa), but the strain hardening and volumetric contraction behaviors are produced at a higher pressure (e.g.,  $p_0 = 1.6$  MPa). Therefore,  $E_{50}$  at  $e_0 = 0.189, 0.244,$  and  $0.285$  can be expressed by Eq. (14a) at a lower pressure (e.g.,  $p_0 = 0.4$  or  $0.8$  MPa) and also by Eq. (14b) at a higher pressure (e.g.,  $p_0 = 1.6$  MPa). A decrease in  $E_{50}$  from the point at  $p_0 = 0.8$  MPa would be caused by a change in the stress-strain relationship from strain softening to strain hardening at  $e_0 = 0.189, 0.244,$  and  $0.285$ . In contrast, TRM at  $e_0 = 0.317$  only exhibits strain hardening and volumetric contraction behaviors. As shown in Fig. 15(b), the secant modulus  $E_{50}$  at 50% of the peak strength decreases with an increase

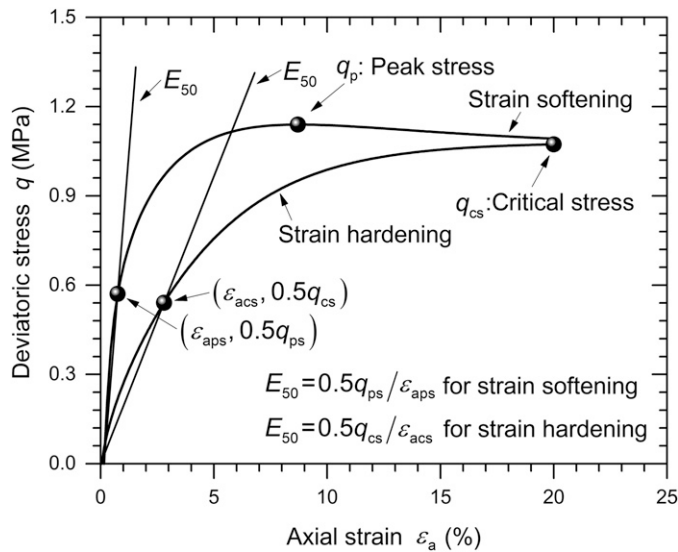


**Fig. 13.** Definition of the secant modulus at 50% of the peak strength

in the initial void ratio. Therefore, the variation in  $E_{50}$  is influenced by the type of stress-strain relationship of TRM.

## Strain Behaviors

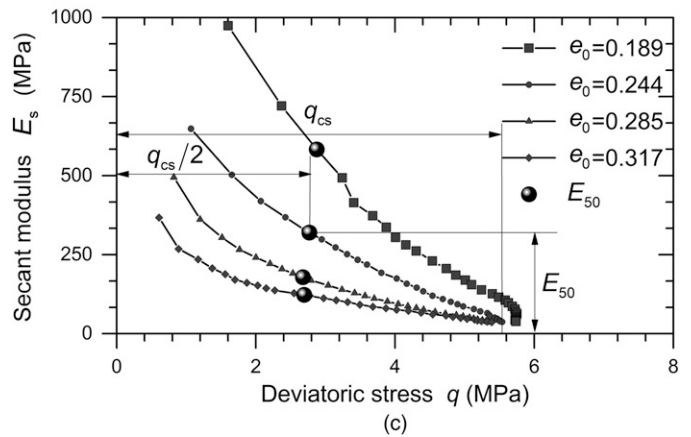
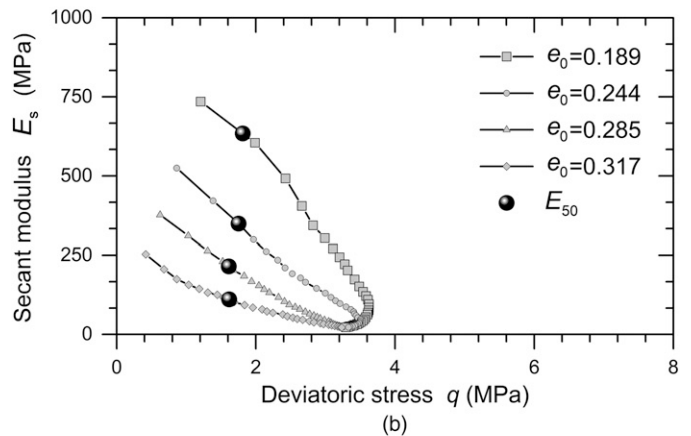
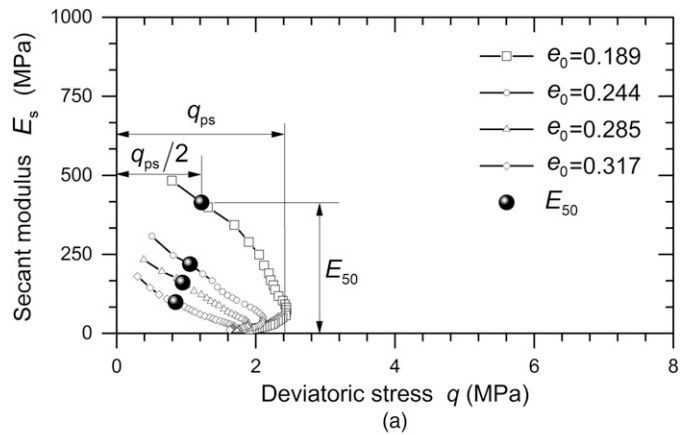
### Stress-Strain Behavior

Fig. 16 illustrates that the stress-strain behavior of TRM at  $e_0 = 0.244$  varies with the initial confining pressure  $p_0$ . As shown in Fig. 16(a), the deviatoric stress at the same axial strain increases with an increase in the initial confining pressure  $p_0$ . TRM exhibits strain-softening behavior at a lower pressure (e.g.,  $p_0 = 0.4$  MPa) and strain-hardening behavior at a higher pressure (e.g.,  $p_0 = 1.6$  MPa), as shown in Fig. 16(a). TRM produces volumetric expansion at  $p_0 = 0.4$  MPa but volumetric contraction at  $p_0 = 1.6$  MPa, as shown in Fig. 16(b). The higher pressure could lead to additional particle breakage, which causes volumetric contraction. The influence of particle breakage on strength and deformation will be introduced in the companion paper (Xiao et al. 2014b).

As shown in Fig. 17, the stress-strain behavior of TRM at  $p_0 = 0.8$  MPa changes with the initial void ratio  $e_0$ . The deviatoric stress at the same axial strain increases with a decrease in the initial void ratio  $e_0$ , as shown in Fig. 17(a). Furthermore, the deviatoric stresses at different initial void ratios coincide with the same critical state deviatoric stress. TRM exhibits strain softening behavior at  $e_0 = 0.189$  but strain hardening behavior at  $e_0 = 0.317$ , as shown in Fig. 17(a). In addition, TRM produces volumetric expansion at  $e_0 = 0.189$  but volumetric contraction at  $e_0 = 0.317$ , as shown in Fig. 17(b). In summary, the stress-strain behavior of TRM is greatly influenced by density and pressure.

### Volumetric Strain

Fig. 18 presents the variation in the volumetric strain of TRM at the end of the test based on the initial void ratio and initial confining pressure. Table 8 presents the values of the volumetric strain  $\epsilon_v$  of TRM at different initial void ratios and initial confining pressures. The volumetric strain at the end of the test is positive for TRM at



**Fig. 14.** Secant modulus of TRM: (a)  $p_0 = 0.4$  MPa; (b)  $p_0 = 0.8$  MPa; (c)  $p_0 = 1.6$  MPa

a larger void ratio (e.g.,  $e_0 = 0.317$ ), as shown in Fig. 18(a), or at a higher confining pressure (e.g.,  $p_0 = 1.6$  MPa), as shown in Fig. 18(b). The positive volumetric strain increases with an increase in the initial void ratio or initial confining pressure. In contrast, the volumetric strain at the end of the test is negative at a smaller void ratio (e.g.,  $e_0 = 0.189$ ) and at a lower confining pressure (e.g.,  $p_0 = 0.4$  MPa).

### Deviatoric Strain

Fig. 19 presents the variation in the deviatoric strain of TRM at the end of the test based on the initial confining pressure [as shown in Fig. 19(a)] and initial void ratio [as shown in Fig. 19(b)]. The values

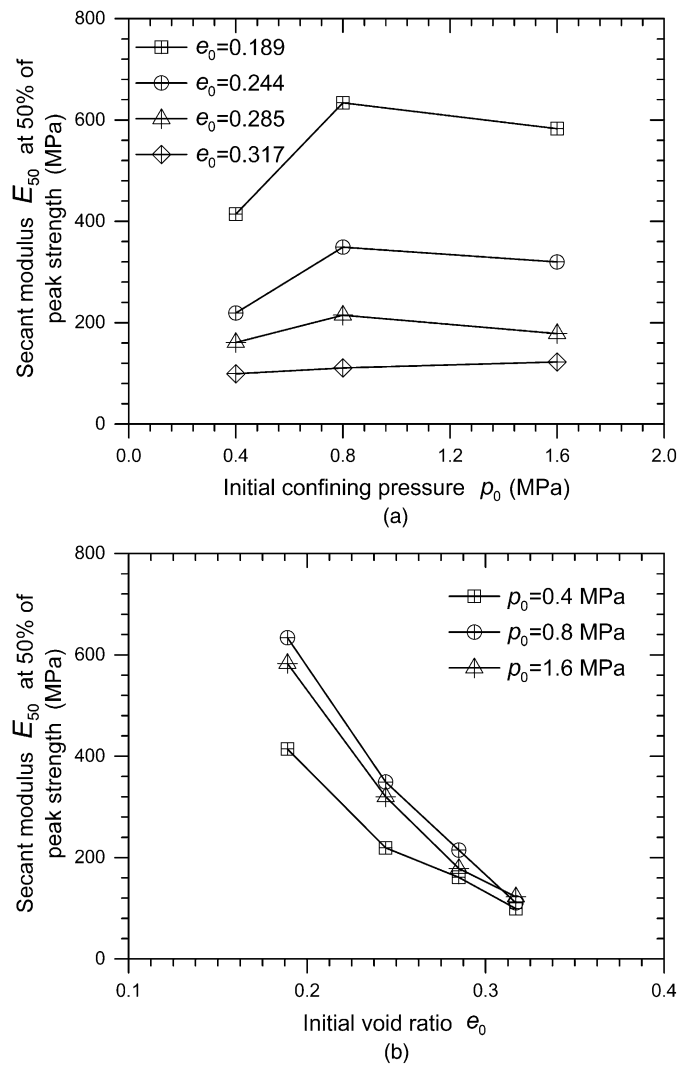


**Fig. 15.** Variations in the secant modulus of TRM at 50% of the peak strength: (a) initial confining pressure; (b) initial void ratio

of the deviatoric strain  $\varepsilon_s$  of TRM at different initial void ratios and initial confining pressures are presented in Table 8. The value of the deviatoric strain ranges from 13 to 17%. An increase in the initial void ratio  $e_0$  or initial confining pressure  $p_0$  can lead to a decrease in the deviatoric strain of TRM.

## CSL

As shown in Fig. 20, the CSL of TRM in the  $e - \lg p'$  space descends with a decrease in the initial void ratio  $e_0$ . The gradient of the CSLs of TRM remains unchanged. The equation of the CSLs in the  $e - \lg p'$  space can be expressed as

$$e_{cs} = e_{cs0} - \lambda \ln p' \quad (15)$$

where  $e_{cs}$  = critical state void ratio;  $e_{cs0}$  = initial critical state void ratio at the unit pressure (Table 9); and compression index  $\lambda$  = gradient of the CSL.

The prediction by Eq. (15) is in good agreement with the test data of TRM at different initial void ratios, as shown in Fig. 20. The initial critical state void ratio at the unit pressure  $e_{cs0}$  varies with  $e_0$ . Similar

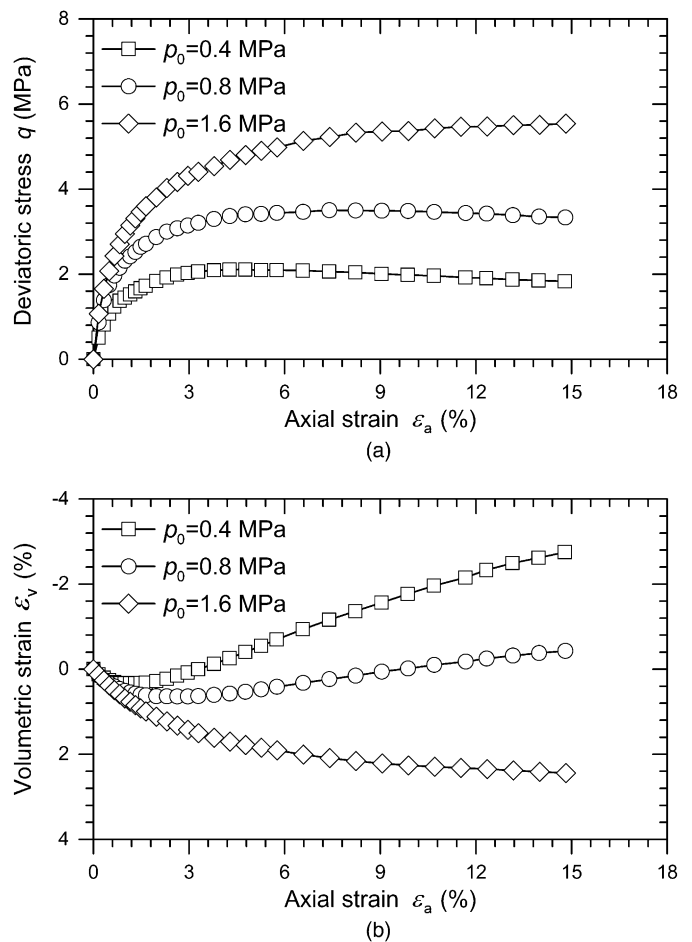


**Fig. 16.** Stress-strain behavior of TRM at  $e_0 = 0.244$ : (a) deviatoric stress versus axial strain; (b) volumetric strain versus axial strain

observations have been made for sands with fines (Yamamuro and Lade 1998; Thevanayagam and Shenthan 2002; Ni et al. 2004; Murthy et al. 2007). The CSLs of sands with fines in the  $e - \lg p'$  space generally descend with an increase in the percentage of fines (percentage smaller than a threshold value), but the gradients of the CSLs of sands mixed with fines remain unchanged. A decrease in the initial void ratio of TRM could result in an increase in particle breakage during the specimen preparation process by vibration, which could be the main reason why the CSLs of TRM descend with an increase in the initial void ratio.

## Conclusions

A series of large-scale triaxial compression tests on TRM were conducted to investigate the influence of density and pressure on the strength and deformation behaviors. The main conclusions can be summarized as follows:

1. Density had a minor influence on the critical state friction angle of TRM. The critical state friction angle of TRM decreased with an increase in the initial confining pressure. The critical state friction angle was expressed as a linear function of the logarithm of the initial confining pressure. An increase in the initial confining pressure or initial void ratio led to a decrease in the peak state friction angle.
2. A revised relative dilatancy index was proposed to capture the influence of density and pressure on the friction angle of TRM

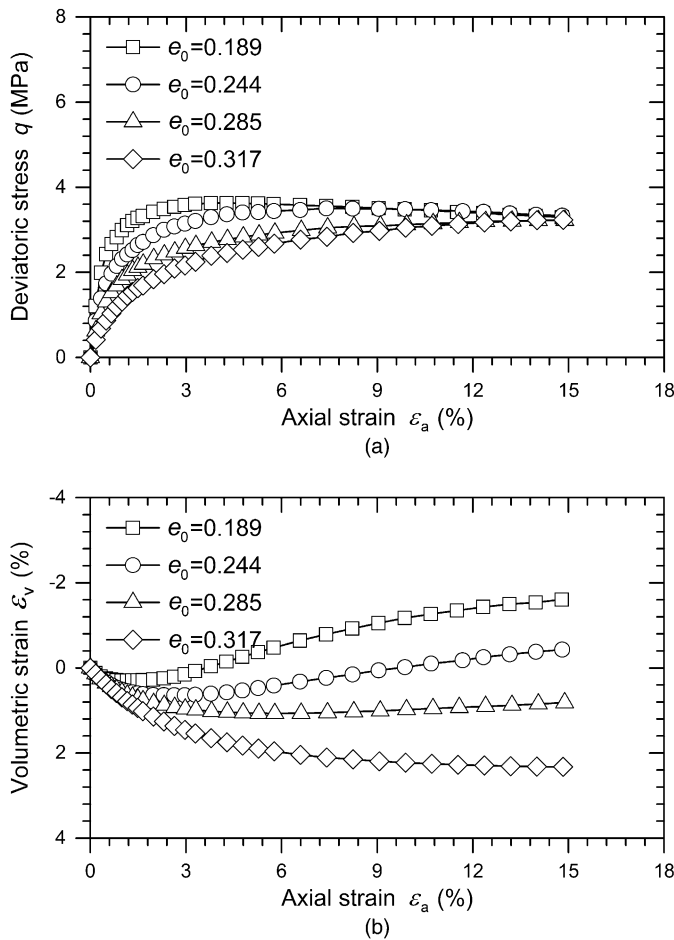


**Fig. 17.** Stress-strain behavior of TRM at  $p_0 = 0.8$  MPa: (a) deviatoric stress versus axial strain; (b) volumetric strain versus axial strain

at the peak failure and characteristic states. The excess peak state friction angle and excess characteristic state friction angle were linearly related to the revised dilatancy index.

3. The initial elastic modulus of TRM at a given initial void ratio increased with an increase in the initial confining pressure, whereas the initial elastic modulus of TRM at a given initial confining pressure decreased with an increase in the initial void ratio. An appropriate equation pertaining to the initial void ratio and initial confining pressure was proposed for the initial elastic modulus.
4. The tangent modulus of TRM at a given initial void ratio and given initial confining pressure decreased with an increase in the deviatoric stress. An increase in the initial void ratio led to a decrease in the tangent modulus at a given deviatoric stress and given initial confining pressure. In addition, an increase in the initial confining pressure resulted in an increase in the tangent modulus at a given deviatoric stress and given initial void ratio.
5. For strain-softening behavior, the secant modulus decreased with an increase in the deviatoric stress up to the peak failure state and then decreased with a decrease in the deviatoric stress. For strain-hardening behavior, the secant modulus decreased with an increase in the deviatoric stress during shearing.
6. TRM presented the behaviors of strain softening and volumetric expansion at a lower confining pressure (e.g.,  $p_0 = 0.4$  MPa) or

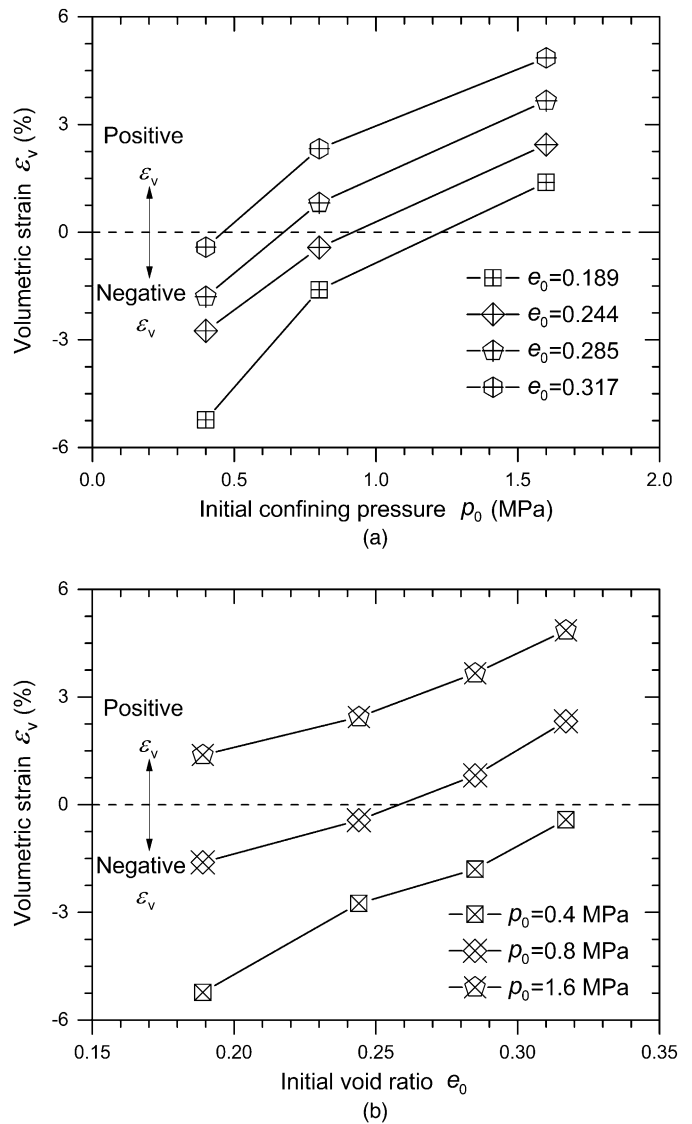


**Fig. 18.** Variations in the volumetric strain of TRM: (a) initial confining pressure; (b) initial void ratio

**Table 8.** Volumetric Strain and Deviatoric Strain of TRM at End of Tests

Initial confining pressure ( $p_0$ ) (MPa)	Initial void ratio ( $e_0$ )	Volumetric strain ( $\epsilon_v$ ) (%)	Deviatoric strain ( $\epsilon_s$ ) (%)
0.4	0.189	-5.23	16.52
	0.244	-2.75	15.71
	0.285	-1.79	15.49
	0.317	-0.42	15.02
0.8	0.189	-1.60	15.33
	0.244	-0.43	14.95
	0.285	0.82	14.61
	0.317	2.33	14.06
1.6	0.189	1.39	14.33
	0.244	2.44	14.01
	0.285	3.66	13.71
	0.317	4.86	13.32

at a smaller void ratio (e.g.,  $e_0 = 0.189$ ). In contrast, it produced strain hardening and volumetric contraction at a higher confining pressure (e.g.,  $p_0 = 1.6$  MPa) or at a larger void ratio (e.g.,  $e_0 = 0.317$ ).

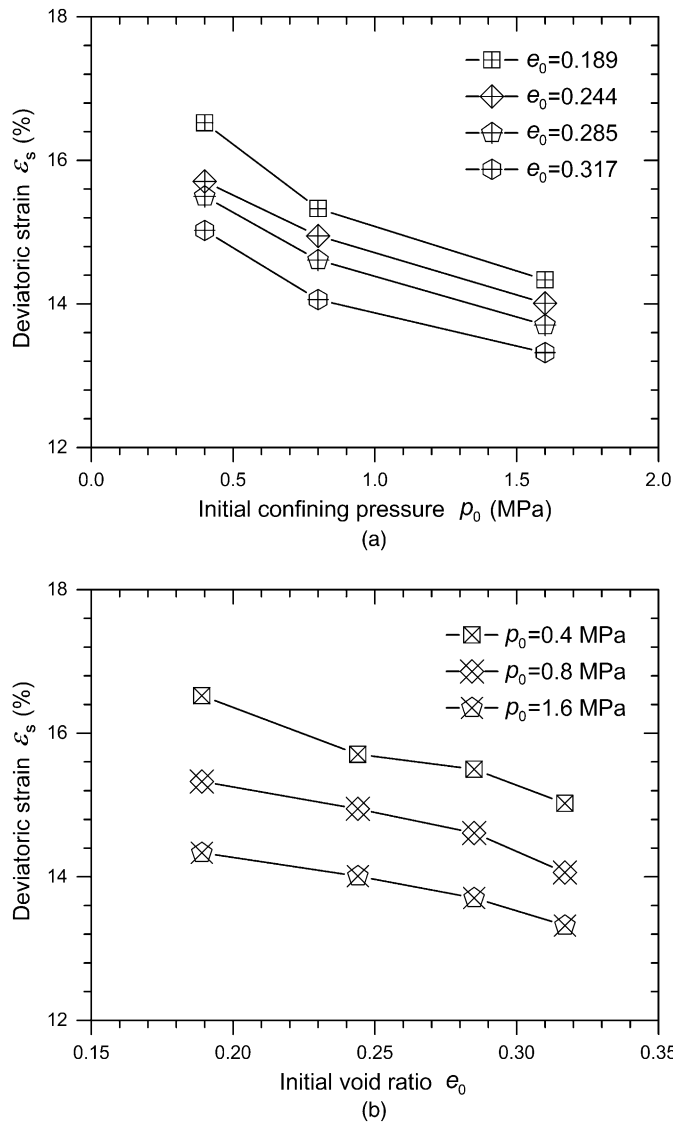


**Fig. 19.** Variations in the deviatoric strain of TRM: (a) initial confining pressure; (b) initial void ratio

7. The volumetric strain of TRM at the end of the test was positive at a higher confining pressure (e.g.,  $p_0 = 1.6$  MPa) and a larger void ratio (e.g.,  $e_0 = 0.317$ ). In contrast, the volumetric strain of TRM at the end of the test was negative at a lower confining pressure (e.g.,  $p_0 = 0.4$  MPa) and a smaller void ratio (e.g.,  $e_0 = 0.189$ ). An increase in the initial void ratio or initial confining pressure resulted in a decrease in the deviatoric strain of TRM.
8. The CSL of TRM in the  $e - \lg p'$  space descended with a decrease in the initial void ratio. The gradient of the CSLs of TRM remained unchanged.

The basic behavior of the strength and deformation for TRM in this study would be the same as that of rockfill materials at other sites. However, some of the material constants may be different for rockfill materials at other sites because of the influence of various factors (e.g., rock type, mineralogy). Therefore, the strength and deformation of rockfill materials depend on the rock type and mineralogy. This will be introduced in future research.

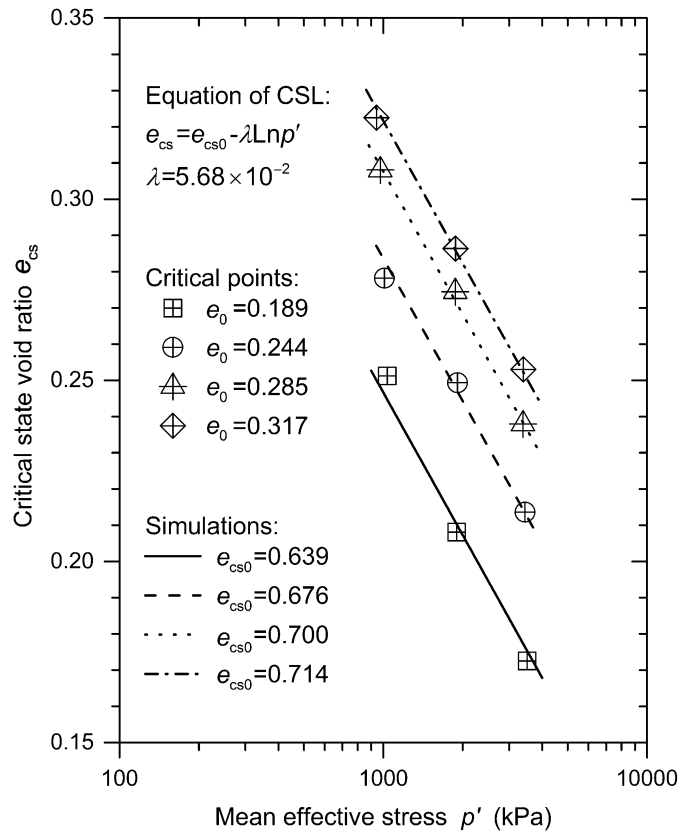


**Fig. 20.** CSL of TRM in the  $e - \lg p'$  space

**Table 9.** Values of Material Constants for Strength and Deformation Behaviors of TRM

Equation	Symbol	Value
Eq. (7)	$\phi_{cs0}$	48.05°
	$\phi_{csd}$	3.10°
Eq. (10)	$Q$	5.39
	$R$	1.53 for Eq. (11) 1.26 for Eq. (12)
Eq. (11)	$\alpha_\phi$	4.69°
Eq. (12)	$\beta_\phi$	3.75°
Eq. (13)	$E_a$	98.43
	$e_E$	0.15
	$\alpha_E$	3
	$\beta_E$	0.5
Eq. (15)	$\lambda$	$5.68 \times 10^{-2}$
	$e_{cs0}$	0.639 for $e_0 = 0.189$ 0.676 for $e_0 = 0.244$ 0.700 for $e_0 = 0.285$ 0.715 for $e_0 = 0.317$

### Acknowledgments

The authors thank the 111 Project (Grant No. B13024), the Program for Changjiang Scholars and Innovative Research Team in University (Grant No. IRT1125), the National Natural Science Foundation of China (Grant No. 51379067), and Fundamental Research Funds for the Central Universities (Grant No. 2011B14514) for their financial support. The authors also thank Dr. W. G. Zhang and Dr. J. He, School of Civil and Environmental Engineering,

## Notation

The following symbols are used in this paper:

- $C_c$  = coefficient of curvature;  
 $C_u$  = coefficient of uniformity;  
 $D_{\max}$  = maximum particle diameter;  
 $D_{10}$  = particle diameter at 10% of grading;  
 $D_{30}$  = particle diameter at 30% of grading;  
 $D_{50}$  = mean particle diameter;  
 $D_{60}$  = particle diameter at 60% of grading;  
 $E_a$  = modulus coefficient;  
 $E_s$  = secant modulus;  
 $E_t$  = tangent modulus;  
 $E_{0i}$  = initial elastic modulus;  
 $E_{50}$  = secant modulus at 50% of the peak strength;  
 $e$  = void ratio;  
 $e_{cs}$  = critical state void ratio;  
 $e_{cs0}$  = initial critical state void ratio at the unit pressure;  
 $e_E$  and  $\alpha_E$  = material constants in relation to the initial void ratio;  
 $e_{\max}$  = maximum void ratio;  
 $e_{\min}$  = minimum void ratio;  
 $e_0$  = initial void ratio;  
 $G_s$  = specific gravity;  
 $I_D$  = relative density;  
 $I_R$  = relative dilatancy index;  
 $I_{RR}$  = revised relative dilatancy index;  
 $p'$  = mean effective stress;  
 $p_a$  = atmospheric pressure;  
 $p_0$  = initial confining pressure;  
 $Q$  and  $R$  = state index constants of material;  
 $q$  = deviatoric stress;  
 $q_{cs}$  = deviatoric stress at the critical state;  
 $q_{ps}$  = deviatoric stress at the peak state;  
 $\alpha_\phi$  = ratio of  $\phi_{ps}^{ex}$  to  $I_{RR}$ ;  
 $\beta_E$  = material constant in relation to the initial confining pressure;  
 $\beta_\phi$  = ratio of  $\phi_{chs}^{ex}$  to  $I_{RR}$ ;  
 $\varepsilon_a$  = axial strain;  
 $\varepsilon_{acs}$  = axial strain at the critical state;  
 $\varepsilon_{aps}$  = axial strain at the peak state;  
 $\varepsilon_s$  = deviatoric strain;  
 $\varepsilon_v$  = volumetric strain;  
 $\eta$  = stress ratio;  
 $\eta_{chs}$  = characteristic state stress ratio;  
 $\eta_{cs}$  = critical state stress ratio;  
 $\eta_{ps}$  = peak state stress ratio;  
 $\lambda$  = compression index;  
 $\rho_d$  = dry density;  
 $\rho_{\max}$  = maximum dry density;  
 $\rho_{\min}$  = minimum dry density;  
 $\sigma'_1, \sigma'_2,$  and  $\sigma'_3$  = major, intermediate, and minor effective principal stresses, respectively;  
 $\phi_{chs}$  = characteristic state friction angle;  
 $\phi_{cs}$  = critical state friction angle;  
 $\phi_{cs0}$  and  $\phi_{csd}$  = material constants;

- $\phi_{chs}^{ex}$  = excess characteristic state friction angle  
 $(=\phi_{cs} - \phi_{chs});$   
 $\phi_{ps}^{ex}$  = excess peak state friction angle  
 $(=\phi_{ps} - \phi_{cs});$   
 $\phi_m$  = mobilized friction angle; and  
 $\phi_{ps}$  = peak state friction angle.

## References

- Anderson, W. F., and Fair, P. (2008). "Behavior of railroad ballast under monotonic and cyclic loading." *J. Geotech. Geoenviron. Eng.*, 10.1061/(ASCE)1090-0241(2008)134:3(316), 316–327.
- Araei, A. A., Razeghi, H. R., Ghalandarzadeh, A., and Tabatabaei, S. H. (2012). "Effects of loading rate and initial stress state on stress–strain behavior of rock fill materials under monotonic and cyclic loading conditions." *Scientia Iranica*, 19(5), 1220–1235.
- ASTM. (2006a). "Standard practice for classification of soils for engineering purposes (Unified Soil Classification System)." *D2487-06*, West Conshohocken, PA.
- ASTM. (2006b). "Standard test method for resistance to degradation of small-size coarse aggregate by abrasion and impact in the Los Angeles machine." *C131-06*, West Conshohocken, PA.
- ASTM. (2006c). "Standard test method for sieve analysis of fine and coarse aggregates." *C136-06*, West Conshohocken, PA.
- ASTM. (2006d). "Standard test methods for uncompacted void content of fine aggregate (as influenced by particle shape, surface texture, and grading)." *C1252-06*, West Conshohocken, PA.
- ASTM. (2010a). "Standard test method for compressive strength and elastic moduli of intact rock core specimens under varying states of stress and temperatures." *D7012-10*, West Conshohocken, PA.
- ASTM. (2010b). "Standard test method for flat particles, elongated particles, or flat and elongated particles in coarse aggregate." *D4791-10*, West Conshohocken, PA.
- ASTM. (2012a). "Standard test method for density, relative density (specific gravity), and absorption of coarse aggregate." *C127-12*, West Conshohocken, PA.
- ASTM. (2012b). "Standard test method for resistance to degradation of large-size coarse aggregate by abrasion and impact in the Los Angeles machine." *C535-12*, West Conshohocken, PA.
- Barton, N., and Kjaernsli, B. (1981). "Shear strength of rockfill." *J. Geotech. Engrg. Div.*, 107(7), 873–891.
- Been, K., and Jefferies, M. G. (1985). "A state parameter for sands." *Géotechnique*, 35(2), 99–112.
- Bolton, M. D. (1986). "The strength and dilatancy of sands." *Géotechnique*, 36(1), 65–78.
- Chakraborty, T., and Salgado, R. (2010). "Dilatancy and shear strength of sand at low confining pressures." *J. Geotech. Geoenviron. Eng.*, 10.1061/(ASCE)GT.1943-5606.0000237, 527–532.
- Charles, J. A., and Watts, K. S. (1980). "The influence of confining pressure on the shear strength of compacted rockfill." *Géotechnique*, 30(4), 353–367.
- Cho, G.-C., Dodds, J., and Santamarina, J. C. (2006). "Particle shape effects on packing density, stiffness, and strength: Natural and crushed sands." *J. Geotech. Geoenviron. Eng.*, 10.1061/(ASCE)1090-0241(2006)132:5(591), 591–602.
- Chu, B. L., Jou, Y. W., and Weng, M. C. (2010). "A constitutive model for gravelly soils considering shear-induced volumetric deformation." *Can. Geotech. J.*, 47(6), 662–673.
- Cooke, J. B. (1984). "Progress in rockfill dams." *J. Geotech. Engrg.*, 10.1061/(ASCE)0733-9410(1984)110:10(1381), 1381–1414.
- Costa, L. M., and Alonso, E. E. (2009). "Predicting the behavior of an earth and rockfill dam under construction." *J. Geotech. Geoenviron. Eng.*, 10.1061/(ASCE)GT.1943-5606.0000058, 851–862.
- Dascal, O. (1987). "Postconstruction deformations of rockfill dams." *J. Geotech. Engrg.*, 10.1061/(ASCE)0733-9410(1987)113:1(46), 46–59.
- Desai, C. S. (2001). *Mechanics of materials and interfaces: The disturbed state concept*, CRC Press, Boca Raton, FL.

- Desai, C. S., and El-Hoseiny, K. E. (2005). "Prediction of field behavior of reinforced soil wall using advanced constitutive model." *J. Geotech. Geoenviron. Eng.*, 10.1061/(ASCE)1090-0241(2005)131:6(729), 729–739.
- Desai, C. S., and Faruque, M. O. (1984). "Constitutive model for (geological) materials." *J. Eng. Mech.*, 10.1061/(ASCE)0733-9399(1984)110:9(1391), 1391–1408.
- Desai, C. S., Jagannath, S. V., and Kundu, T. (1995). "Mechanical and ultrasonic anisotropic response of soil." *J. Eng. Mech.*, 10.1061/(ASCE)0733-9399(1995)121:6(744), 744–752.
- Desai, C. S., Janardhanam, R., and Sture, S. (1982). "High capacity multiaxial testing device." *ASTM Geotech. Test. J.*, 5(1/2), 26–33.
- Desai, C. S., and Salami, M. R. (1987). "Constitutive model for rocks." *J. Geotech. Engrg.*, 10.1061/(ASCE)0733-9410(1987)113:5(407), 407–423.
- Desai, C. S., and Siriwardane, H. J. (1983). *Constitutive laws for engineering materials*, Prentice Hall, Englewood Cliffs, NJ.
- Desai, C. S., and Toth, J. (1996). "Disturbed state constitutive modeling based on stress-strain and nondestructive behavior." *Int. J. Solids Struct.*, 33(11), 1619–1650.
- Diyaljee, V. A. (1987). "Effects of stress history on ballast deformation." *J. Geotech. Engrg.*, 10.1061/(ASCE)0733-9410(1987)113:8(909), 909–914.
- Duncan, J. M., and Chang, C.-Y. (1970). "Nonlinear analysis of stress and strain in soils." *J. Soil Mech. and Found. Div.*, 96(5), 1629–1653.
- Elgamal, A.-W. (1992). "Three-dimensional seismic analysis of La Villita dam." *J. Geotech. Engrg.*, 10.1061/(ASCE)0733-9410(1992)118:12(1937), 1937–1958.
- European Committee for Standardization (CEN). (2010). "Tests for mechanical and physical properties of aggregates methods for the determination of resistance to fragmentation." *EN 1097-2*, Brussels, Belgium.
- Flores-Berrones, R., Ramírez-Reynaga, M., and Macari, E. J. (2011). "Internal erosion and rehabilitation of an earth-rock dam." *J. Geotech. Geoenviron. Eng.*, 10.1061/(ASCE)GT.1943-5606.0000371, 150–160.
- Frossard, E., Dano, C., Hu, W., and Hicher, P. Y. (2012). "Rockfill shear strength evaluation: A rational method based on size effects." *Géotechnique*, 62(5), 415–427.
- Fu, Z., Chen, S., and Peng, C. (2014). "Modeling cyclic behavior of rockfill materials in a framework of generalized plasticity." *Int. J. Geomech.*, 10.1061/(ASCE)GM.1943-5622.0000302, 191–204.
- Gajo, A., and Muir Wood, D. (1999). "Severn–Trent sand: A kinematic-hardening constitutive model: The q–p formulation." *Géotechnique*, 49(5), 595–614.
- Gudehus, G. (1996). "A comprehensive constitutive equation for granular materials." *Soils Found.*, 36(1), 1–12.
- Gupta, A. K. (2000). "Constitutive modeling of rockfill materials." Ph.D. thesis, Indian Institute of Technology, Delhi, India.
- Gupta, A. K. (2009a). "Effect of particle size and confining pressure on breakage and strength parameters of rockfill materials." *Electron. J. Geotech. Eng.*, 14(Bund. H), 1–12.
- Gupta, A. K. (2009b). "Triaxial behaviour of rockfill materials." *Electron. J. Geotech. Eng.*, 14(Bund. J), 1–18.
- Haque, A., Kabir, E., and Bouazza, A. (2007). "Cyclic filtration apparatus for testing subballast under rail track." *J. Geotech. Geoenviron. Eng.*, 10.1061/(ASCE)1090-0241(2007)133:3(338), 338–341.
- Honkanadavar, N. P. (2010). *Testing and modeling the behaviour of modeled and prototype rockfill materials*, Indian Institute of Technology, Delhi, India.
- Honkanadavar, N. P., and Gupta, S. L. (2010). "Prediction of shear strength parameters for prototype riverbed rockfill material using index properties." *Indian Geotechnical Conf.*, Indian Geotechnical Society, New Delhi, India, 335–338.
- Honkanadavar, N. P., Gupta, S. L., and Bajaj, S. (2011). "Deformability characteristics of quarried rockfill material." *Int. J. Earth Sci. Eng.*, 4(6), 128–131.
- Honkanadavar, N. P., Gupta, S. L., and Ratnam, M. (2012). "Effect of particle size and confining pressure on shear strength parameter of rockfill materials." *Int. J. Adv. Civil Eng. Archit.*, 1(1), 49–63.
- Hu, L., Zhang, B., and Ma, J. (2010). "Mechanical characteristics for interfaces between granular materials." *Mech. Res. Commun.*, 37(1), 42–46.
- Hunter, G., and Fell, R. (2003). "Rockfill modulus and settlement of concrete face rockfill dams." *J. Geotech. Geoenviron. Eng.*, 10.1061/(ASCE)1090-0241(2003)129:10(909), 909–917.
- Indraratna, B., Ionescu, D., and Christie, H. D. (1998). "Shear behavior of railway ballast based on large-scale triaxial tests." *J. Geotech. Geoenviron. Eng.*, 10.1061/(ASCE)1090-0241(1998)124:5(439), 439–449.
- Ishihara, K. (1993). "Liquefaction and flow failure during earthquakes." *Géotechnique*, 43(3), 351–451.
- Ishihara, K., Tatsuoka, F., and Yasuda, S. (1975). "Undrained deformation and liquefaction of sand under cyclic stresses." *Soils Found.*, 15(1), 29–44.
- Janardhanam, R., and Desai, C. S. (1983). "Three-dimensional testing and modeling of ballast." *J. Geotech. Engrg.*, 10.1061/(ASCE)0733-9410(1983)109:6(783), 783–796.
- Jiang, J. S. (2009). "Experimental research on micro-characteristics and deformation mechanism for coarse-grained soils." Ph.D. thesis, Hohai Univ., Nanjing, China.
- Khalid, S., Singh, B., Nayak, G. C., and Jain, O. P. (1990). "Nonlinear analysis of concrete face rockfill dam." *J. Geotech. Engrg.*, 10.1061/(ASCE)0733-9410(1990)116:5(822), 822–837.
- Lashkari, A. (2009). "On the modeling of the state dependency of granular soils." *Comput. Geotech.*, 36(7), 1237–1245.
- Leps, T. M. (1970). "Review of shearing strength of rockfill." *J. Soil Mech. and Found. Div.*, 96(4), 1159–1170.
- Li, X. S. (1997). "Modeling of dilative shear failure." *J. Geotech. Geoenviron. Eng.*, 10.1061/(ASCE)1090-0241(1997)123:7(609), 609–616.
- Li, X. S., and Dafalias, Y. F. (2000). "Dilatancy for cohesionless soils." *Géotechnique*, 50(4), 449–460.
- Li, X. S., and Dafalias, Y. F. (2002). "Constitutive modeling of inherently anisotropic sand behavior." *J. Geotech. Geoenviron. Eng.*, 10.1061/(ASCE)1090-0241(2002)128:10(868), 868–880.
- Li, X. S., and Wang, Y. (1998). "Linear representation of steady-state line for sand." *J. Geotech. Geoenviron. Eng.*, 10.1061/(ASCE)1090-0241(1998)124:12(1215), 1215–1217.
- Loukidis, D., and Salgado, R. (2009). "Modeling sand response using two-surface plasticity." *Comput. Geotech.*, 36(1–2), 166–186.
- Lowe, J. (1964). "Shear strength of coarse embankment dam materials." *Proc., 8th Int. Congress on Large Dams*, International Commission on Large Dams, Paris, 745–761.
- Luong, M. P. (1980). "Stress-strain aspects of cohesionless soils under cyclic and transient loading." *Proc., Int. Symp. Soils under Cyclic and Transient Loading*, A. A. Balkema, Rotterdam, Netherlands, 315–324.
- Marsal, R. J. (1967). "Large-scale testing of rockfill materials." *J. Soil Mech. and Found. Div.*, 93(2), 27–43.
- Marschi, N. D., Chan, C. K., and Seed, H. B. (1972). "Evaluation of properties of rockfill materials." *J. Soil Mech. and Found. Div.*, 98(1), 95–114.
- Matheson, G. M. (1986). "Relationship between compacted rockfill density and gradation." *J. Geotech. Engrg.*, 10.1061/(ASCE)0733-9410(1986)112:12(1119), 1119–1124.
- McDowell, G. R., and Bolton, M. D. (1998). "On the micromechanics of crushable aggregates." *Géotechnique*, 48(5), 667–679.
- McDowell, G. R., Bolton, M. D., and Robertson, D. (1996). "The fractal crushing of granular materials." *J. Mech. Phys. Solids*, 44(12), 2079–2102.
- Milligan, V. (2003). "Some uncertainties in embankment dam engineering." *J. Geotech. Geoenviron. Eng.*, 10.1061/(ASCE)1090-0241(2003)129:9(785), 785–797.
- Murthy, T. G., Loukidis, D., Carraro, J. H., Prezzi, M., and Salgado, R. (2007). "Undrained monotonic response of clean and silty sands." *Géotechnique*, 57(3), 273–288.
- Ni, Q., Tan, T. S., Dasari, G. R., and Hight, D. W. (2004). "Contribution of fines to the compressive strength of mixed soils." *Géotechnique*, 54(9), 561–569.
- Nimbalkar, S., Indraratna, B., Dash, S. K., and Christie, D. (2012). "Improved performance of railway ballast under impact loads using shock mats." *J. Geotech. Geoenviron. Eng.*, 10.1061/(ASCE)GT.1943-5606.0000598, 281–294.
- Papalou, A., and Bielak, J. (2004). "Nonlinear seismic response of earth dams with canyon interaction." *J. Geotech. Geoenviron. Eng.*, 10.1061/(ASCE)1090-0241(2004)130:1(103), 103–110.

- Peiris, L. M. N., Madabhushi, S. P. G., and Schofield, A. N. (2008). "Centrifuge modeling of rock-fill embankments on deep loose saturated sand deposits subjected to earthquakes." *J. Geotech. Geoenviron. Eng.*, 10.1061/(ASCE)1090-0241(2008)134:9(1364), 1364–1374.
- Prato, C. A., and Matheu, E. E. (1991). "Simplified seismic analysis of embankment dams-canyon-wall configuration." *J. Geotech. Engrg.*, 10.1061/(ASCE)0733-9410(1991)117:11(1802), 1802–1808.
- Roscoe, K. H., Schofield, A. N., and Thurairajah, A. (1963). "Yielding of clays in states wetter than critical." *Géotechnique*, 13(3), 211–240.
- Rowe, P. W. (1962). "The stress-dilatancy relation for static equilibrium of an assembly of particles in contact." *Proc., R. Soc. Lond. A Math. Phys. Sci.*, 269(1339), 500–527.
- Schofield, A. N., and Wroth, C. P. (1968). *Critical state soil mechanics*, McGraw Hill, London.
- Seif El Dine, B., Dupla, J. C., Frank, R., Canou, J., and Kazan, Y. (2010). "Mechanical characterization of matrix coarse-grained soils with a large-sized triaxial device." *Can. Geotech. J.*, 47(4), 425–438.
- Seo, M.-W., Ha, I. S., Kim, Y.-S., and Olson, S. M. (2009). "Behavior of concrete-faced rockfill dams during initial impoundment." *J. Geotech. Geoenviron. Eng.*, 10.1061/(ASCE)GT.1943-5606.0000021, 1070–1081.
- Sevi, A., and Ge, L. (2012). "Cyclic behaviors of railroad ballast within the parallel gradation scaling framework." *J. Mater. Civ. Eng.*, 10.1061/(ASCE)MT.1943-5533.0000460, 797–804.
- Shi, W. C. (2008). "True triaxial tests on coarse-grained soils and study on constitutive model." Ph.D. thesis, Hohai Univ., Nanjing, China.
- Simoni, A., and Housby, G. T. (2006). "The direct shear strength and dilatancy of sand–gravel mixtures." *Geotech. Geol. Eng.*, 24(3), 523–549.
- Tatsuoka, F., and Ishihara, K. (1974). "Drained deformation of sand under cyclic stresses reversing direction." *Soils Found.*, 14(3), 51–65.
- Thevanayagam, S., Shenthan, T., Mohan, S., and Liang, J. (2002). "Undrained fragility of clean sands, silty sands, and sandy silts." *J. Geotech. Geoenviron. Eng.*, 10.1061/(ASCE)1090-0241(2002)128:10(849), 849–859.
- Uddin, N., and Gazetas, G. (1995). "Dynamic response of concrete-faced rockfill dams to strong seismic excitation." *J. Geotech. Engrg.*, 10.1061/(ASCE)0733-9410(1995)121:2(185), 185–197.
- Varadarajan, A., Sharma, K. G., Abbas, S. M., and Dhawan, A. K. (2006). "Constitutive model for rockfill materials and determination of material constants." *Int. J. Geomech.*, 10.1061/(ASCE)1532-3641(2006)6:4(226), 226–237.
- Varadarajan, A., Sharma, K. G., Venkatachalam, K., and Gupta, A. K. (1997). "Constitutive modeling of a rockfill material using HISS model." *Proc., Indian Geotechnical Conf.*, New Delhi, India, 153–156.
- Varadarajan, A., Sharma, K. G., Venkatachalam, K., and Gupta, A. K. (1999). "Constitutive modelling of a rockfill materials." *Proc., 4th Int. Conf. on Constitutive Laws for Engineering Materials*, Rensselaer Polytechnic Institute, Troy, NY.
- Varadarajan, A., Sharma, K. G., Venkatachalam, K., and Gupta, A. K. (2003). "Testing and modeling two rockfill materials." *J. Geotech. Geoenviron. Eng.*, 10.1061/(ASCE)1090-0241(2003)129:3(206), 206–218.
- Vasistha, Y., Gupta, A. K., and Kanwar, V. (2012). "Prediction of shear strength parameters of two rockfill materials." *Electron. J. Geotech. Eng.*, 17(Bund. W), 3221–3232.
- Vasistha, Y., Gupta, A. K., and Kanwar, V. (2013). "Medium triaxial testing of some rockfill materials." *Electron. J. Geotech. Eng.*, 18(Bund. D), 923–964.
- Walberg, F. C., et al. (2013). "Seismic retrofit of Tuttle Creek dam." *J. Geotech. Geoenviron. Eng.*, 10.1061/(ASCE)GT.1943-5606.0000818, 975–986.
- Wan, R. G., and Guo, P. J. (1999). "A pressure and density dependent dilatancy model for granular materials." *Soils Found.*, 39(6), 1–11.
- Wang, Z.-L., Dafalias, Y. F., Li, X.-S., and Makdisi, F. I. (2002). "State pressure index for modeling sand behavior." *J. Geotech. Geoenviron. Eng.*, 10.1061/(ASCE)1090-0241(2002)128:6(511), 511–519.
- Xiao, Y., Liu, H., Chen, Y., and Jiang, J. (2014a). "Bounding surface plasticity model incorporating the state pressure index for rockfill materials." *J. Eng. Mech.*, 10.1061/(ASCE)EM.1943-7889.0000802, 04014087.
- Xiao, Y., Liu, H., Chen, Y., and Jiang, J. (2014b). "Strength and deformation of rockfill material based on large-scale triaxial compression tests. II: Influence of particle breakage." *J. Geotech. Geoenviron.*, 10.1061/(ASCE)GT.1943-5606.0001177, 04014071.
- Xiao, Y., Liu, H., Chen, Y., Jiang, J., and Zhang, W. (2014c). "State-dependent constitutive model for rockfill materials." *Int. J. Geomech.*, 10.1061/(ASCE)GM.1943-5622.0000421, 04014075.
- Xiao, Y., Liu, H. L., Zhu, J. G., and Shi, W. C. (2011a). "Dilatancy equation of rockfill material under the true triaxial stress condition." *Sci. China Tech. Sci.*, 54(S1), 175–184.
- Xiao, Y., Liu, H. L., Zhu, J. G., and Shi, W. C. (2012). "Modeling and behaviours of rockfill materials in three-dimensional stress space." *Sci. China Tech. Sci.*, 55(10), 2877–2892.
- Xiao, Y., Liu, H. L., Zhu, J. G., Shi, W. C., and Liu, M. C. (2011b). "A 3D bounding surface model for rockfill materials." *Sci. China Tech. Sci.*, 54(11), 2904–2915.
- Xing, H.-F., Gong, X.-N., Zhou, X.-G., and Fu, H.-F. (2006). "Construction of concrete-faced rockfill dams with weak rocks." *J. Geotech. Geoenviron. Eng.*, 10.1061/(ASCE)1090-0241(2006)132:6(778), 778–785.
- Xu, M., Song, E., and Chen, J. (2012). "A large triaxial investigation of the stress-path-dependent behavior of compacted rockfill." *Acta Geotech.*, 7(3), 167–175.
- Yamamoto, J. A., and Lade, P. V. (1998). "Steady-state concepts and static liquefaction of silty sands." *J. Geotech. Geoenviron. Eng.*, 10.1061/(ASCE)1090-0241(1998)124:9(868), 868–877.
- Yang, J., and Li, X. S. (2004). "State-dependent strength of sands from the perspective of unified modeling." *J. Geotech. Geoenviron. Eng.*, 10.1061/(ASCE)1090-0241(2004)130:2(186), 186–198.
- Yao, Y. P., Sun, D. A., and Luo, T. (2004). "A critical state model for sands dependent on stress and density." *Int. J. Numer. Anal. Met.*, 28(4), 323–337.